

Dictionary Learning with Low-rank Coding Coefficients for Tensor Completion

Tai-Xiang Jiang, Xi-Le Zhao, Hao Zhang, Michael K. Ng*

arXiv:2009.12507v1 [cs.CV] 26 Sep 2020

Abstract—In this paper, we propose a novel tensor learning and coding model for third-order data completion. Our model is to learn a data-adaptive dictionary from the given observations, and determine the coding coefficients of third-order tensor tubes. In the completion process, we minimize the low-rankness of each tensor slice containing the coding coefficients. By comparison with the traditional pre-defined transform basis, the advantages of the proposed model are that (i) the dictionary can be learned based on the given data observations so that the basis can be more adaptively and accurately constructed, and (ii) the low-rankness of the coding coefficients can allow the linear combination of dictionary features more effectively. Also we develop a multi-block proximal alternating minimization algorithm for solving such tensor learning and coding model, and show that the sequence generated by the algorithm can globally converge to a critical point. Extensive experimental results for real data sets such as videos, hyperspectral images, and traffic data are reported to demonstrate these advantages and show the performance of the proposed tensor learning and coding method is significantly better than the other tensor completion methods in terms of several evaluation metrics.

Index Terms—Tensor completion, dictionary learning, tensor singular value decomposition (t-SVD), low-rank coding.

I. INTRODUCTION

TENSOR completion is a problem of filling the missing or unobserved entries of the incomplete observed data, playing an important role in a wide range of real-world applications, such as color image inpainting [1–4], high-speed compressive video [5], magnetic resonance imaging (MRI) data recovery [6], and hyperspectral data inpainting [7]. Generally, many real-world tensors are inner correlated, the spectral redundancy [8] of the hyperspectral images (HSIs) for example. Therefore, it is effective to utilize the global low-dimensional structure to characterize the relationship between the missing entries and observed ones.

* Corresponding author.

This work is supported in part by the Fundamental Research Funds for the Central Universities (JBK2001011 and JBK2001035), in part by the National Natural Science Foundation of China (61772003 and 61876203), in part by the HKRGC GRF (12306616, 12200317, 12300218, 12300519, and 17201020), and in part by the HKU Grant 104005583.

T.-X. Jiang is with FinTech Innovation Center, School of Economic Information Engineering, Southwestern University of Finance and Economics, Chengdu, Sichuan, P.R.China (e-mail: taixiangjiang@gmail.com, jiangtx@swufe.edu.cn).

X.-L. Zhao and H. Zhang are with Research Center for Image and Vision Computing, School of Mathematical Sciences, University of Electronic Science and Technology of China, Chengdu 611731, P.R.China (e-mail: xlzhao122003@163.com; 201821110218@std.uestc.edu.cn).

M. K. Ng is with Department of Mathematics, The University of Hong Kong, Pokfulam, Hong Kong (e-mail: mng@maths.hku.hk).

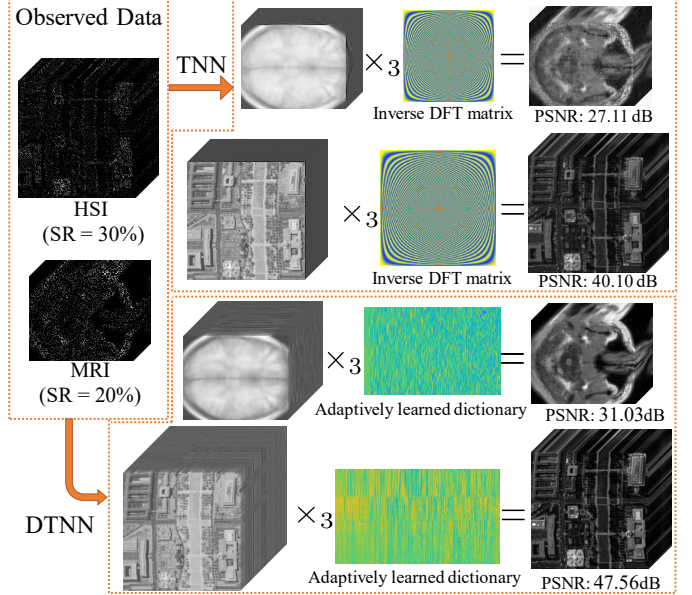


Fig. 1. An illustration of the TNN based LRTC and the DTNN based LRTC. SR denotes the sampling rate.

Generally, like the matrix case, the low-rank tensor completion (LRTC) can be formulated as

$$\min \text{rank}(\mathcal{X}) \quad \text{s.t. } \mathcal{X}_\Omega = \mathcal{O}_\Omega, \quad (1)$$

where \mathcal{X} is the underlying tensor, \mathcal{O} is the observed incomplete tensor as shown in the top-left of Fig. 1, Ω is the index set corresponding to the observed entries, and $\mathcal{X}_\Omega = \mathcal{O}_\Omega$ enforces the entries of \mathcal{X} in Ω equal to the observation \mathcal{O} . However, unlike the matrix cases, the definition of the tensor rank is still not unique and has received considerable attentions in recent researches. This work fixes attentions on a novel notion of the tensor rank, i.e., the tubal-rank, which is derived from the tensor singular value decomposition (t-SVD) framework [9, 10].

For a third-order tensor $\mathcal{X} \in \mathbb{R}^{n_1 \times n_2 \times n_3}$, its t-SVD is given as $\mathcal{X} = \mathcal{U} * \mathcal{S} * \mathcal{V}^H$, where \mathcal{U} and \mathcal{V} are orthogonal tensors (see Def. 3) of size $n_1 \times n_1 \times n_3$ and $n_2 \times n_2 \times n_3$ respectively, and $*$ denotes the t-prod (see Def. 2). The tubal-rank of \mathcal{X} is defined as the number of non-zero singular tubes of \mathcal{S} . Since that the LRTC problem associated with the tubal-rank is NP-hard, Zhang *et al.* [11] turn to minimize the tensor nuclear norm (TNN), which is a convex surrogate of the tubal-rank, and give some theoretical guarantees. The TNN based LRTC

model is given as

$$\min \| \mathcal{X} \|_{\text{TNN}} \quad \text{s.t. } \mathcal{X}_{\Omega} = \mathcal{O}_{\Omega}. \quad (2)$$

The t-prod is based on a convolution-like operation and can be implemented using the discrete Fourier transform (DFT) [12]. Consequently, the TNN can be computed by using the DFT matrix. More specifically, for $\mathcal{X} \in \mathbb{R}^{n_1 \times n_2 \times n_3}$, after respectively denoting the DFT matrix and inverse DFT matrix as \mathbf{F}_{n_3} and $\mathbf{F}_{n_3}^{-1}$, its Fourier transformed (along the third mode) tensor $\mathcal{Z} \in \mathbb{C}^{n_1 \times n_2 \times n_3}$ can be obtained by $\mathcal{Z} = \mathcal{X} \times_3 \mathbf{F}_{n_3}$, where \times_3 is the tensor-matrix product (See Sec. II-B), and we have $\mathcal{X} = \mathcal{Z} \times_3 \mathbf{F}_{n_3}^{-1}$. Then, $\| \mathcal{X} \|_{\text{TNN}} = \| \text{bdiag}(\mathcal{Z}) \|_* = \sum_{k=1}^{n_3} \| \mathcal{Z}(:, :, k) \|_*$, where $\text{bdiag}(\cdot)$ is the block diagonal operation (see Def. 5). Thus, (2) is equivalent to

$$\min_{\mathcal{Z}} \| \text{bdiag}(\mathcal{Z}) \|_* \quad \text{s.t. } (\mathcal{Z} \times_3 \mathbf{F}_{n_3}^{-1})_{\Omega} = \mathcal{O}_{\Omega}. \quad (3)$$

As shown in the top-right of Fig. 1, the TNN based LTRC model can be comprehended as finding the coding coefficients tensor \mathcal{Z} , which is slice-wisely low-rank, of \mathcal{X} with a predefined dictionary $\mathbf{F}_{n_3}^{-1}$.

From the transform perspective, Kernfeld *et al.* [12] note that the t-SVD framework can be defined via any invertible transform. The TNN in (2) can be alternatively implemented by using other transform, e.g., the discrete cosine transform (DCT) adopted by Lu *et al.* [13] and Xu *et al.* [14], and the Haar wavelet transform exploited in [15]. Furthermore, Jiang *et al.* [16] introduce the framelet transform, which is semi-invertible, and break through the restriction of invertibility. Nonetheless, all these methods can be rewritten in the form of (3) and interpreted as to find a slice-wisely low-rank coding \mathcal{Z} of the original tensor \mathcal{X} with some predefined dictionaries, e.g., the inverse DCT transform matrix and the inverse framelet transform matrix. Within these transform based TNN methods, the typical pipeline is applying one selected transform along the third dimension, and minimizing the low-rankness of slices of the transformed data (coefficients) for the completion. Once the tubes of the original tensor are highly correlated, the frontal slices of the transformed data would be low-rank [15, 16].

An unavoidable issue is that the correlations along the third mode are different for various types of data. For example, the redundancy of HSIs along the third mode are much higher than videos with changing scenes. Thus, predefined dictionaries, viz the inverse transform matrices, usually lack flexibility and could not be suitable for all kinds of data. Therefore, to address this issue, we construct a dictionary, which can be adaptively inferred from the data, instead of inverse transform matrices mentioned above. We formulate the LTRC model as

$$\min_{\mathcal{Z}, \mathbf{D}} \| \text{bdiag}(\mathcal{Z}) \|_* \quad \text{s.t. } (\mathcal{Z} \times_3 \mathbf{D})_{\Omega} = \mathcal{O}_{\Omega}, \quad (4)$$

where $\mathbf{D} \in \mathbb{R}^{n_3 \times d}$ (generally $d \gg n_3$). To avoid the situation where the elements in \mathbf{D} reach arbitrarily high values allowing for arbitrarily low (but non-zero) values of \mathcal{Z} , we additionally constrain \mathbf{D} 's columns as $\| \mathbf{D}(:, i) \|_2 = 1$ for $i = 1, 2, \dots, d$.

The bottom-right part in Fig. 1 shows the coefficients and the dictionaries obtained by our method. We can see that the dictionary learned for the HSI completion is smoother than that

for the MRI data. The front slices of the original data \mathcal{X} are linear combinations of front slices of the coefficients tensor \mathcal{Z} . Meanwhile, as the number of atoms in \mathbf{D} is much bigger than the length of the tubes, the low-rank representation of tensor tubes is expected to be more efficiently. With the adaptively learned dictionary and corresponding low-rank coding, the performance of our method is significant better than the TNN based LTRC method (see the peak signal-to-noise ratio (PSNR) values exhibited in Fig. 1).

As mentioned by the authors of [13, 15], it is interesting to learn the transform for implementing the t-SVD from the data in different tasks. Our approach can be viewed as learning the inverse transform from this perspective and indeed enriches the research on this topic. The methods, which utilize DFT, DCT, and Framelet, can be viewed as specific instances of our method with fixed dictionaries, i.e., the inverse discrete transformation matrices. From the view of dictionary learning, our method can also be interpreted as learning a dictionary with low-rank coding. We enforce the low-rankness of the coding coefficients in a tensor manner, and this allows the linear combination of features, namely, the atoms of the dictionary.

The main contributions of this paper mainly consist of three aspects:

- We propose novel tensor learning and coding model, which is to adaptively learn a dictionary from the observations and determine the low rank coding coefficients, for the third-order tensor completion.
- A multi-block proximal alternating minimization algorithm is designed to solve the proposed non-convex model. We theoretically prove its global convergence to a critical point.
- Extensive experiments are conducted on various types of real-world third-order tensor data. The results illustrate that our method outperforms compared LTRC methods.

This paper is organized as follows. Sec. II introduces related works and the basic preliminaries. Our method is given in Sec. III. We report the experimental results in Sec. IV. Finally, Sec. V draws some conclusions.

II. RELATED WORK AND PRELIMINARIES

A. Related Work

The t-SVD framework is proposed in [9, 10] and it induces the definition of the tubal-rank. Zhang *et al.* [11] utilize the TNN, which is the convex relaxation of the tubal-rank, for LTRC problems and give theoretical bounds from limited sampling for third-order tensor recovery in their journal extension [17]. Jiang *et al.* [18] and Wang *et al.* [19] tackle the robust tensor completion task, in which the incomplete observations are corrupted by sparse outliers, via minimizing TNN. In [13, 15, 16], other transformations are selected as substitutes of the DFT to formulate the transform based TNN and the corresponding LTRC models.

As mentioned before, different kinds of tensor rank notions exist and have also been widely investigated. For instance, the CANDECOMP/PARAFAC (CP)-rank, based on the CP decomposition, is defined as the minimal rank-one tensors to

express the original data [20]. Although determining the CP-rank of a given tensor is NP-hard [21], CP decomposition have been successfully applied for tensor recovery problem [22–24]. The Tucker-rank, corresponding to the Tucker decomposition [25], is defined as a vector constituted of the ranks of the unfolding matrices. Liu *et al.* [4] propose a convex surrogate of the Tucker-rank and minimize it for the LRTC problem while Zhang *et al.* [26] resort to use a family of nonconvex functions onto the singular values. Another newly emerged one is the tensor train (TT)-rank derived from the TT decomposition [27]. In this framework, the tensor is decomposed in a chain manner with nodes being third-order tensors. Bengua *et al.* [28] minimize a nuclear norm based on the TT-rank for the color image and video recovery. The TT-rank has also been applied for the HSI super-resolution [29] and the tensor-on-tensor regression [30]. When factors cyclically connected, it becomes the tensor ring (TR) decomposition [31]. Yuan *et al.* [32] exploit the low-rank structure of the TR latent space and regularize the latent TR factors with the nuclear norm. Yu *et al.* [33] introduce the tensor circular unfolding for the TR decomposition and perform parallel low-rank matrix factorizations to all circularly unfolded matrices for tensor completion. For a comprehensive overview of the LRTC problem, please refer to [34, 35].

B. Preliminaries

Throughout this paper, lowercase letters, e.g., x , boldface lowercase letters, e.g., \mathbf{x} , boldface upper-case letters, e.g., \mathbf{X} , and boldface calligraphic letters, e.g., \mathcal{X} , are used to denote scalars, vectors, matrices, and tensors, respectively. Given a third-order tensor $\mathcal{X} \in \mathbb{R}^{n_1 \times n_2 \times n_3}$, we use \mathcal{X}_{ijk} to denote its (i, j, k) -th element. The k -th frontal slice of \mathcal{X} is denoted as $\mathcal{X}^{(k)}$ (or $\mathcal{X}(:, :, k)$, \mathbf{X}^k), and the mode-3 unfolding matrix of \mathcal{X} is denoted as $\mathbf{X}_{(3)} \in \mathbb{R}^{n_3 \times n_1 n_2}$. We use fold_3 and unfold_3 to denote the folding and unfolding operations along the third dimension, respectively, and we have $\mathcal{X} = \text{fold}_3(\text{unfold}_3(\mathcal{X})) = \text{fold}_3(\mathbf{X}_{(3)})$. The mode-3 tensor-matrix product is denoted as \times_3 , and we have $\mathcal{X} \times_3 \mathbf{A} \Leftrightarrow \text{Aunfold}_3(\mathcal{X})$. The tensor Frobenius norm of a third-order tensor \mathcal{X} is defined as $\|\mathcal{X}\|_F := \sqrt{\langle \mathcal{X}, \mathcal{X} \rangle} = \sqrt{\sum_{ijk} \mathcal{X}_{ijk}^2}$.

Definition 1 (tensor conjugate transpose [36]). *The conjugate transpose of a tensor $\mathcal{A} \in \mathbb{C}^{n_2 \times n_1 \times n_3}$ is tensor $\mathcal{A}^H \in \mathbb{C}^{n_1 \times n_2 \times n_3}$ obtained by conjugate transposing each of the frontal slice and then reversing the order of transposed frontal slices 2 through n_3 , i.e., $(\mathcal{A}^H)^{(1)} = (\mathcal{A}^{(1)})^H$ and $(\mathcal{A}^H)^{(i)} = (\mathcal{A}^{(n_3+2-i)})^H$ ($i = 2, \dots, n_3$).*

Definition 2 (t-prod [36]). *The tensor-tensor-product (t-prod) $\mathcal{C} = \mathcal{A} * \mathcal{B}$ of $\mathcal{A} \in \mathbb{R}^{n_1 \times n_2 \times n_3}$ and $\mathcal{B} \in \mathbb{R}^{n_2 \times n_4 \times n_3}$ is a tensor of size $n_1 \times n_4 \times n_3$, where the (i, j) -th tube $\mathbf{c}_{ij:}$ is given by*

$$\mathbf{c}_{ij:} = \mathcal{C}(i, j, :) = \sum_{k=1}^{n_2} \mathcal{A}(i, k, :) * \mathcal{B}(k, j, :) \quad (5)$$

where $*$ denotes the circular convolution between two tubes of same size.

Definition 3 (special tensors [36]). *The identity tensor $\mathcal{I} \in \mathbb{R}^{n_1 \times n_1 \times n_3}$ is the tensor whose first frontal slice is the $n_1 \times n_1$ identity matrix, and whose other frontal slices are all zeros. A tensor $\mathcal{Q} \in \mathbb{C}^{n_1 \times n_1 \times n_3}$ is orthogonal if it satisfies*

$$\mathcal{Q}^H * \mathcal{Q} = \mathcal{Q} * \mathcal{Q}^H = \mathcal{I}. \quad (6)$$

A tensor \mathcal{A} is called **f-diagonal** if each frontal slice $\mathcal{A}^{(i)}$ is a diagonal matrix.

Theorem 1 (t-SVD [10, 36]). *For $\mathcal{A} \in \mathbb{R}^{n_1 \times n_2 \times n_3}$, the t-SVD of \mathcal{A} is given by*

$$\mathcal{A} = \mathcal{U} * \mathcal{S} * \mathcal{V}^H \quad (7)$$

where $\mathcal{U} \in \mathbb{R}^{n_1 \times n_1 \times n_3}$ and $\mathcal{V} \in \mathbb{R}^{n_2 \times n_2 \times n_3}$ are orthogonal tensors, and $\mathcal{S} \in \mathbb{R}^{n_1 \times n_2 \times n_3}$ is an f-diagonal tensor.

Definition 4 (tensor tubal-rank [11]). *The tubal-rank of a tensor $\mathcal{A} \in \mathbb{R}^{n_1 \times n_2 \times n_3}$, denoted as $\text{rank}_t(\mathcal{A})$, is defined to be the number of non-zero singular tubes of \mathcal{S} , where \mathcal{S} comes from the t-SVD of \mathcal{A} : $\mathcal{A} = \mathcal{U} * \mathcal{S} * \mathcal{V}^T$. That is $\text{rank}_t(\mathcal{A}) = \#\{i : \mathcal{S}(i, :, :) \neq 0\}$.*

Definition 5 (block diagonal operation [11]). *The block diagonal operation of $\mathcal{A} \in \mathbb{R}^{n_1 \times n_2 \times n_3}$ is given by*

$$\text{bdiag}(\mathcal{A}) \triangleq \begin{bmatrix} \mathcal{A}^{(1)} & & & \\ & \mathcal{A}^{(2)} & & \\ & & \ddots & \\ & & & \mathcal{A}^{(n_3)} \end{bmatrix}, \quad (8)$$

where, and $\text{bdiag}(\mathcal{A}) \in \mathbb{C}^{n_1 n_3 \times n_2 n_3}$.

Definition 6 (tensor-nuclear-norm (TNN) [11]). *The tensor nuclear norm of a tensor $\mathcal{A} \in \mathbb{R}^{n_1 \times n_2 \times n_3}$, denoted as $\|\mathcal{A}\|_{\text{TNN}}$, is defined as*

$$\|\mathcal{A}\|_{\text{TNN}} \triangleq \|\text{bdiag}(\mathcal{Z})\|_*, \quad (9)$$

where $\mathcal{Z} \in \mathbb{R}^{n_1 \times n_2 \times n_3}$ is the Fourier transformed (along the third mode) tensor of \mathcal{A} . The TNN can be computed via the summation of the matrix nuclear norm of \mathcal{Z} 's frontal slices. That is $\|\mathcal{A}\|_{\text{TNN}} = \sum_{i=1}^{n_3} \|\mathcal{Z}(:, :, i)\|_*$.

III. MAIN RESULTS

A. Proposed Model

The proposed tensor learning and coding model is formulated as

$$\begin{aligned} \min_{\mathcal{Z}, \mathbf{D}} \quad & \|\text{bdiag}(\mathcal{Z})\|_*, \\ \text{s.t.} \quad & (\mathcal{Z} \times_3 \mathbf{D})_\Omega = \mathcal{O}_\Omega \\ & \|\mathbf{D}(:, i)\|_2 = 1 \text{ for } i = 1, 2, \dots, d, \end{aligned} \quad (10)$$

where $\mathbf{D} \in \mathbb{R}^{n_3 \times d}$ and $\mathcal{Z} \in \mathbb{R}^{n_1 \times n_2 \times d}$ are respective the dictionary and the low-rank coding coefficients. Since that our LRTC model is very similar to the TNN based model in (3), we term it as dictionary based TNN (DTNN)¹.

¹We remark here that, although the objective function of (10) is in the same form of TNN in (3), it could not be derived to a normative definition of a norm as Def. 6. Given a tensor \mathcal{X} and a certain dictionary \mathbf{D} , the coefficients in \mathcal{Z} here could not be directly obtained and satisfy $(\mathcal{Z} \times_3 \mathbf{D}) = \mathcal{X}$. It is needed to optimize (10) simultaneously with respect to the dictionary and coefficients (with Ω indexing all the entries).

While resembling (3) in form, our model in (10) is distinct from the TNN based LRTC model. The main deference is that our model is more flexible for different kinds of data because of the data-adaptive dictionary term. The dictionary used in (10) can be viewed as the inverse transform. This is also different from previous works tailoring the linear or unitary transform [13, 15].

Traditional dictionary learning techniques utilize overcomplete dictionaries, the amount of whose atoms is always more than the dimension of the signal, and find the sparse representations [37]. In (10), although d is much bigger than n_3 , \mathbf{D} is still not big enough to overcompletely represent \mathcal{X} , which is of big volume, with sparse coefficients. Therefore, we need the specific low-rank structure of the coefficients, which allows the linear combination of features, together with the learned dictionary, to accurately complete \mathcal{X} . Thus, our method is distinct from previous tensor dictionary learning methods, which enforce the sparsity of coefficients, e.g., [38]. Please see Sec. IV-E1 for detailed comparisons of sparsity and low-rankness.

B. Proposed Algorithm

To optimize the specific structured problem in the proposed model, we tailored a multi-block proximal alternating minimization algorithm. Let

$$\Phi(\mathcal{X}) = \begin{cases} 0, & \mathcal{X}_\Omega = \mathcal{O}_\Omega, \\ \infty, & \text{otherwise,} \end{cases}$$

and

$$\Psi(\mathbf{D}) = \begin{cases} 0, & \|\mathbf{D}(:, i)\|_2 = 1 \text{ for } i = 1, 2, \dots, d, \\ \infty, & \text{otherwise.} \end{cases}$$

Thus, the problem in (10) can be rewritten as the following unconstraint problem

$$\min_{\mathcal{Z}, \mathbf{D}} \Phi(\mathcal{Z} \times_3 \mathbf{D}) + \sum_{k=1}^d \|\mathcal{Z}^{(k)}\|_* + \Psi(\mathbf{D}) \quad (11)$$

(11) is difficult to be directly optimized. Therefore, we resort to the half quadratic splitting (HQS) technique and turn to solve the following problem

$$\min_{\mathcal{Z}, \mathbf{D}, \mathcal{X}} \frac{\beta}{2} \|\mathcal{X} - \mathcal{Z} \times_3 \mathbf{D}\|_F^2 + \Phi(\mathcal{X}) + \sum_{k=1}^d \|\mathcal{Z}^{(k)}\|_* + \Psi(\mathbf{D}). \quad (12)$$

We denote the objective function in (12) as $L(\mathcal{Z}, \mathbf{D}, \mathcal{X})$. Then, we update each variable alternatively via:

$$\begin{aligned} \mathcal{Z}_{k+1} &\in \arg \min_{\mathcal{Z}} \left\{ L(\mathcal{Z}, \mathbf{D}_k, \mathcal{X}_k) + \frac{\rho_k^z}{2} \|\mathcal{Z} - \mathcal{Z}_k\|_F^2 \right\}, \\ \mathbf{D}_{k+1} &\in \arg \min_{\mathbf{D}} \left\{ L(\mathcal{Z}_{k+1}, \mathbf{D}, \mathcal{X}_k) + \frac{\rho_k^d}{2} \|\mathbf{D} - \mathbf{D}_k\|_F^2 \right\}, \\ \mathcal{X}_{k+1} &\in \arg \min_{\mathcal{X}} \left\{ L(\mathcal{Z}_{k+1}, \mathbf{D}_{k+1}, \mathcal{X}) + \frac{\rho_k^x}{2} \|\mathcal{X} - \mathcal{X}_k\|_F^2 \right\}, \end{aligned} \quad (13)$$

where $(\rho_k^z)_{k \in \mathbb{N}}$, $(\rho_k^d)_{k \in \mathbb{N}}$, and $(\rho_k^x)_{k \in \mathbb{N}}$ are three positive sequences.

1) *Updating \mathcal{Z} and \mathbf{D}* : Following the updating strategy in [39], the coefficient \mathcal{Z} (or equivalently denoted as $\mathbf{Z}_{(3)}$ for simplification) and the dictionary \mathbf{D} can be respectively decomposed as followings:

$$\mathbf{Z}_{(3)} = \begin{bmatrix} \mathbf{z}^1 \\ \vdots \\ \mathbf{z}^i \\ \vdots \\ \mathbf{z}^d \end{bmatrix} = \begin{bmatrix} \text{vec}(\mathbf{Z}^1)^\top \\ \vdots \\ \text{vec}(\mathbf{Z}^i)^\top \\ \vdots \\ \text{vec}(\mathbf{Z}^d)^\top \end{bmatrix} = \begin{bmatrix} \text{vec}(\mathcal{Z}(:, :, 1))^\top \\ \vdots \\ \text{vec}(\mathcal{Z}(:, :, i))^\top \\ \vdots \\ \text{vec}(\mathcal{Z}(:, :, d))^\top \end{bmatrix} \quad (14)$$

and

$$\mathbf{D}_k = [\mathbf{d}_k^1, \dots, \mathbf{d}_k^i, \dots, \mathbf{d}_k^d], \quad (15)$$

where $\mathbf{Z}^i = \mathcal{Z}(:, :, i)$ indicates the i -th frontal slice of the tensor \mathcal{Z} , $\mathbf{z}^i = \text{vec}(\mathbf{Z}^i)$, and $\mathbf{d}^i = \mathbf{D}(:, i)$ is the i -th atom of \mathbf{D} . Thus, the \mathcal{Z} subproblem and the \mathbf{D} subproblem can be respectively split into d problems. Then, we update the pair of \mathbf{Z}^i and \mathbf{d}^i from $i = 1$ to d . This updating scheme is the same as the well-known KSVD technique [40].

Firstly, we define

$$\begin{cases} \mathbf{Z}^{k,i} = [\mathbf{z}_{k+1}^1, \dots, \mathbf{z}_{k+1}^{i-1}, \mathbf{z}_{k+1}^{i+1}, \dots, \mathbf{z}_{k+1}^d]^\top, \\ \mathbf{D}^{k,i} = [\mathbf{d}_{k+1}^1, \dots, \mathbf{d}_{k+1}^{i-1}, \mathbf{d}_k^{i+1}, \dots, \mathbf{d}_k^d], \\ \mathbf{R}^{k,i} = \text{unfold}_3(\mathcal{X}_k) - \mathbf{D}^{k,i} \mathbf{Z}^{k,i}, \\ \mathbf{M}^{k,i} = \frac{\rho_k^z \mathbf{Z}_k^i + \beta \text{vec}^{-1}((\mathbf{R}^{k,i})^\top \mathbf{d}_k^i)}{\beta + \rho_k^z}, \\ \mathbf{p}^{k,i} = \beta \mathbf{R}^{k,i} \text{vec}(\mathcal{Z}_k(:, :, i)) + \rho_k^d \mathbf{d}_k^i. \end{cases} \quad (16)$$

The \mathbf{Z}^i and \mathbf{d}^i ($i = 1, \dots, d$) subproblems are respectively as following:

$$\min_{\mathbf{Z}^i} \frac{\beta}{2} \|\mathbf{R}^{k,i} - \mathbf{d}_k^i \mathbf{z}^{i\top}\|_F^2 + \|\mathbf{Z}^i\|_* + \frac{\rho_k^z}{2} \|\mathbf{Z}^i - \mathbf{Z}_k^i\|_F^2, \quad (17)$$

and

$$\min_{\mathbf{d}^i} \frac{\beta}{2} \|\mathbf{R}^{k,i} - \mathbf{d}^i \mathbf{z}_{k+1}^{i\top}\|_F^2 + \Psi(\mathbf{D}) + \frac{\rho_k^d}{2} \|\mathbf{d}^i - \mathbf{d}_k^i\|_F^2. \quad (18)$$

Note that two quadratic terms in (17) can be combined as

$$\begin{aligned} &\frac{\beta}{2} \|\mathbf{R}^{k,i} - \mathbf{d}_k^i (\mathbf{z}^i)^\top\|_F^2 + \frac{\rho_k^z}{2} \|\mathbf{Z}^i - \mathbf{Z}_k^i\|_F^2 \\ &= \frac{\beta}{2} (\langle \mathbf{R}^{k,i}, \mathbf{R}^{k,i} \rangle - 2 \langle \mathbf{R}^{k,i}, \mathbf{d}_k^i (\mathbf{z}^i)^\top \rangle + \langle \mathbf{d}_k^i (\mathbf{z}^i)^\top, \mathbf{d}_k^i (\mathbf{z}^i)^\top \rangle) \\ &\quad + \frac{\rho_k^z}{2} (\langle \mathbf{Z}^i, \mathbf{Z}^i \rangle - 2 \langle \mathbf{Z}^i, \mathbf{Z}_k^i \rangle + \langle \mathbf{Z}_k^i, \mathbf{Z}_k^i \rangle) \\ &= \frac{\beta}{2} (\langle \mathbf{R}^{k,i}, \mathbf{R}^{k,i} \rangle - 2 \langle \text{vec}^{-1}((\mathbf{R}^{k,i})^\top \mathbf{d}_k^i), \mathbf{Z}^i \rangle + \langle \mathbf{Z}^i, \mathbf{Z}^i \rangle) \\ &\quad + \frac{\rho_k^z}{2} (\langle \mathbf{Z}^i, \mathbf{Z}^i \rangle - 2 \langle \mathbf{Z}^i, \mathbf{Z}_k^i \rangle + \langle \mathbf{Z}_k^i, \mathbf{Z}_k^i \rangle) \\ &= \frac{\beta + \rho_k^z}{2} \|\mathbf{Z}^i - \frac{\rho_k^z \mathbf{Z}_k^i + \beta \text{vec}^{-1}((\mathbf{R}^{k,i})^\top \mathbf{d}_k^i)}{\beta + \rho_k^z} \mathbf{Z}_k^i\|_F^2 + \frac{\rho_k^z}{2} \|\mathbf{Z}_k^i\|_F^2 \\ &\quad - \frac{1}{2(\beta + \rho_k^z)} \|\rho_k^z \mathbf{Z}_k^i + \beta \text{vec}^{-1}((\mathbf{R}^{k,i})^\top \mathbf{d}_k^i)\|_F^2 + \frac{\beta}{2} \|\mathbf{R}^{k,i}\|_F^2, \end{aligned}$$

where vec^{-1} denotes the inverse reshaping operation of vec in (14). Therefore, leaving terms independent of \mathbf{Z}^i and adding

the nuclear norm term, the minimization problem in (17) is equivalent to:

$$\mathbf{Z}_{k+1}^i \in \arg \min_{\mathbf{Z}^i} \|\mathbf{Z}^i\|_* + \frac{\beta + \rho_k^z}{2} \|\mathbf{Z}^i - \mathbf{M}^{k,i}\|_F^2, \quad (19)$$

where $\mathbf{M}^{k,i} = \frac{\rho_k^z \mathbf{Z}_k^i + \beta \text{vec}^{-1}((\mathbf{R}^{k,i})^\top \mathbf{d}^i)}{\beta + \rho_k^z}$. Then, we can directly derive the closed form solution of (19) with the singular value thresholding (SVT) operator [41] as

$$\mathbf{Z}_{k+1}^i = \text{SVT}_{\frac{1}{\beta + \rho_k^z}}(\mathbf{M}^{k,i}) \triangleq \mathbf{U} \left(\mathbf{S} - \frac{1}{\beta + \rho_k^z} \right)_+ \mathbf{V}^\top, \quad (20)$$

where $(\mathbf{U}, \mathbf{S}, \mathbf{V})$ comes from the SVD of $\mathbf{M}^{k,i}$, \mathbf{S} is a diagonal matrix with $\mathbf{M}^{k,i}$'s singular values, and $(\cdot)_+$ means keeping the positive values and setting the negative values as 0

Similarly, we can obtain the closed form solution of (18) as following:

$$\mathbf{d}_{k+1}^i = (\|\mathbf{p}^{k,i}\|_2)^{-1} \mathbf{p}^{k,i}. \quad (21)$$

Afterwards, we obtain the \mathcal{Z}_{k+1} with its i -th frontal slice equal to \mathbf{Z}_{k+1}^i and $\mathbf{D}_{k+1} = [\mathbf{d}_{k+1}^1, \dots, \mathbf{d}_{k+1}^i, \dots, \mathbf{d}_{k+1}^d]$.

2) *Updating \mathcal{X} :* We update \mathcal{X} via solving the following minimization problem:

$$\min_{\mathcal{X}} \frac{\beta}{2} \|\mathcal{X} - \mathcal{Z}_{k+1} \times_3 \mathbf{D}_{k+1}\|_F^2 + \Phi(\mathcal{X}) + \frac{\rho_k^x}{2} \|\mathcal{X} - \mathcal{X}_k\|_F^2.$$

\mathcal{X}_{k+1} is updated via the following steps:

$$\begin{cases} \mathcal{X}_{k+\frac{1}{2}} = \frac{\beta \text{fold}_3(\mathbf{D}_{k+1} \mathbf{Z}_{k+1(3)}) + \rho_k^x \mathcal{X}_k}{\beta + \rho_k^x}, \\ \mathcal{X}_{k+1} = (\mathcal{X}_{k+\frac{1}{2}})_{\Omega^C} + \mathcal{O}_{\Omega}. \end{cases} \quad (22)$$

Finally, the pseudocode to solve (12) is summarized in Algorithm 1. The computation complexity of our algorithm at each iteration is $O(dn_1n_2(dn_3 + \min(n_1, n_2) + n_3))$, given an input with size $n_1 \times n_2 \times n_3$.

Algorithm 1 Proximal alternating minimization algorithm for solving (12)

Input: The observed tensor $\mathcal{O} \in \mathbb{R}^{n_1 \times n_2 \times n_3}$; the set of observed entries Ω .

Initialization: $\mathcal{X}^{(0)}$, \mathbf{D}^0 , and \mathbf{Z}^0 ;

1: **while** not converged **do**
2: **for** $i = 1$ to d **do**
3: Update $\mathcal{Z}^{k+1}(:, :, i)$ via Eq. (19);
4: Update $\mathbf{D}^{k+1}(:, i)$ via (21);
5: **end for**
6: Update \mathcal{X}^k (22).
7: **end while**

Output: The reconstructed tensor \mathcal{X} .

C. Convergency analysis

In this part, we are really to establish the theoretical guarantee of convergence on our algorithm. We first define K-L functions and semi-algebraic functions, which provide the basic ingredients for the convergence analysis.

Definition 7. (Kurdyka-Łojasiewicz property [42]) A proper lower semi-continuous function $f : \mathbb{R}^n \rightarrow \mathbb{R} \cup +\infty$ is said

to have the K-L property at $\bar{x} \in \text{dom}(\partial f)$ if there exist $\eta \in (0, +\infty]$, a neighborhood U of \bar{x} and a continuous concave function $\phi : [0, \eta] \rightarrow [0, +\infty]$, which satisfies $\phi(0) = 0$, ϕ is C^1 on $(0, \eta)$, and $\phi(s) > 0, \forall s \in (0, \eta)$ such that for each $x \in U \cap [f(\bar{X}) < f < f(\bar{x}) + \eta]$ the K-L inequality holds:

$$\phi(f(x) - f(\bar{x})) \text{dist}(0, \partial f(x)) \geq 1. \quad (23)$$

If f satisfy the K-L property at each point of $\text{dom} \partial f$ then f is called a K-L function.

Definition 8. (Semi-algebraic sets and functions [42]) A subset S of \mathbb{R} is called the semi-algebraic set if there exists a finite number of real polynomial functions g_{ij}, h_{ij} such that $S = \bigcap_j \bigcup_i \{x \in \mathbb{R}^n : g_{ij}(x) = 0, h_{ij}(x) < 0\}$. A function f is called the semi-algebraic function if its graph $\{(x, t) \in \mathbb{R}^n \times \mathbb{R}, t = f(x)\}$ is a semi-algebraic set.

Lemma 1. ([43]) A semi-algebraic real valued function f is a K-L function, i.e., f satisfies K-L property at each $x \in \text{dom}(f)$.

For convenience, we define the following formularies,

$$\begin{aligned} F(\mathcal{Z}) &= \sum_{k=1}^d \|\mathcal{Z}^{(k)}\|_* = \|\text{bdiag}(\mathcal{Z})\|_*, \\ \delta_{\mathcal{X}}(\mathcal{X}) &= \Phi(\mathcal{X}), \\ \delta_{\mathcal{D}}(\mathbf{D}) &= \Psi(\mathbf{D}), \\ Q(\mathcal{Z}, \mathbf{D}, \mathcal{X}) &= \frac{\beta}{2} \|\mathcal{Z} - \mathcal{Z} \times_3 \mathbf{D}\|_F^2, \\ L(\mathcal{Z}, \mathbf{D}_k, \mathcal{X}_k) &= F(\mathcal{Z}) + \delta_{\mathcal{X}}(\mathcal{X}) + \delta_{\mathcal{D}}(\mathbf{D}) + Q(\mathcal{Z}, \mathbf{D}, \mathcal{X}), \end{aligned}$$

and

$$\begin{cases} \mathcal{Z}_{k+1} \in \arg \min_{\mathcal{Z}} \{M_1(\mathcal{Z} | \mathcal{Z}^k) := F(\mathcal{Z}) \\ \quad + Q(\mathcal{Z}, \mathbf{D}_k, \mathcal{X}_k) + \frac{\rho_k^z}{2} \|\mathcal{Z} - \mathcal{Z}_k\|_F^2\}, \\ \mathbf{D}_{k+1} \in \arg \min_{\mathbf{D}} \{M_2(\mathbf{D} | \mathbf{D}^k) := \delta_{\mathcal{D}}(\mathcal{X}) \\ \quad + Q(\mathcal{Z}_{k+1}, \mathbf{D}, \mathcal{X}_k) + \frac{\rho_k^d}{2} \|\mathbf{D} - \mathbf{D}_k\|_F^2\}, \\ \mathcal{X}_{k+1} \in \arg \min_{\mathcal{X}} \{M_3(\mathcal{X} | \mathcal{X}^k) := \delta_{\mathcal{X}}(\mathcal{X}) \\ \quad + Q(\mathcal{Z}_{k+1}, \mathbf{D}_{k+1}, \mathcal{X}) + \frac{\rho_k^x}{2} \|\mathcal{X} - \mathcal{X}_k\|_F^2\}. \end{cases} \quad (24)$$

We first begin to show a descent Lemma for $L(\mathcal{Z}, \mathbf{D}_k, \mathcal{X}_k)$.

Lemma 2 (Descent Lemma). Assume that $L(\mathcal{Z}, \mathbf{D}_k, \mathcal{X}_k)$ is a C^1 function with locally Lipschitz continuous gradient and $\rho_k^z, \rho_k^d, \rho_k^x > 0$. Let $\{\mathcal{Z}_k, \mathbf{D}_k, \mathcal{X}_k\}_{k \in \mathbb{N}}$ is generated by (24). Then

$$\begin{aligned} F(\mathcal{Z}_{k+1}) + Q(\mathcal{Z}_{k+1}, \mathbf{D}_k, \mathcal{X}_k) + \frac{\rho_k^z}{2} \|\mathcal{Z}_{k+1} - \mathcal{Z}_k\|_F^2 &\leq \\ F(\mathcal{Z}_k) + Q(\mathcal{Z}_k, \mathbf{D}_k, \mathcal{X}_k), \\ \delta_{\mathcal{D}}(\mathbf{D}_{k+1}) + Q(\mathcal{Z}_{k+1}, \mathbf{D}_{k+1}, \mathcal{X}_k) + \frac{\rho_k^d}{2} \|\mathbf{D}_{k+1} - \mathbf{D}_k\|_F^2 &\leq \\ \delta_{\mathcal{D}}(\mathbf{D}_k) + Q(\mathcal{Z}_{k+1}, \mathbf{D}_k, \mathcal{X}_k), \\ \delta_{\mathcal{X}}(\mathcal{X}_{k+1}) + Q(\mathcal{Z}_{k+1}, \mathbf{D}_{k+1}, \mathcal{X}_{k+1}) + \frac{\rho_k^x}{2} \|\mathcal{X}_{k+1} - \mathcal{X}_k\|_F^2 &\leq \\ \delta_{\mathcal{X}}(\mathcal{X}_k) + Q(\mathcal{Z}_{k+1}, \mathbf{D}_{k+1}, \mathcal{X}_k). \end{aligned}$$

Proof. When \mathbf{D}_{k+1} and \mathcal{Z}_{k+1} are optimal solutions of M_2 and M_3 , $\delta_{\mathcal{D}} = 0$ and $\delta_{\mathcal{X}} = 0$. By the definitions of M_1, M_2 , and M_3 , we clearly have that

$$\begin{aligned} F(\mathcal{Z}_{k+1}) + Q(\mathcal{Z}_{k+1}, \mathbf{D}_k, \mathcal{X}_k) + \frac{\rho_k^z}{2} \|\mathcal{Z}_{k+1} - \mathcal{Z}_k\|_F^2 \\ = M_1(\mathcal{Z}_{k+1} | \mathcal{Z}_k) \leq M_1(\mathcal{Z}_k | \mathcal{Z}_k) \\ = F(\mathcal{Z}_k) + Q(\mathcal{Z}_k, \mathbf{D}_k, \mathcal{X}_k), \\ \delta_{\mathcal{D}}(\mathbf{D}_{k+1}) + Q(\mathcal{Z}_{k+1}, \mathbf{D}_{k+1}, \mathcal{X}_k) + \frac{\rho_k^d}{2} \|\mathbf{D}_{k+1} - \mathbf{D}_k\|_F^2 \\ = M_2(\mathbf{D}_{k+1} | \mathbf{D}_k) \leq M_2(\mathbf{D}_k | \mathbf{D}_k) \\ = \delta_{\mathcal{D}}(\mathbf{D}_k) + Q(\mathcal{Z}_{k+1}, \mathbf{D}_k, \mathcal{X}_k), \\ \delta_{\mathcal{X}}(\mathcal{X}_{k+1}) + Q(\mathcal{Z}_{k+1}, \mathbf{D}_{k+1}, \mathcal{X}_{k+1}) + \frac{\rho_k^x}{2} \|\mathcal{X}_{k+1} - \mathcal{X}_k\|_F^2 \\ = M_3(\mathcal{X}_{k+1} | \mathcal{X}_k) \leq M_3(\mathcal{X}_k | \mathcal{X}_k) \\ = \delta_{\mathcal{X}}(\mathcal{X}_k) + Q(\mathcal{Z}_{k+1}, \mathbf{D}_{k+1}, \mathcal{X}_k). \end{aligned}$$

The descent lemma has been proved. \square

Then, we show the relative error Lemma.

Lemma 3 (Relative error Lemma). $\{\mathcal{Z}_k, \mathbf{D}_k, \mathcal{X}_k\}_{k \in \mathbb{N}}$ is generated by (24) and $\rho_k^z, \rho_k^d, \rho_k^x > 0$. Then there exists $V_{1,k+1}, V_{2,k+1}, V_{3,k+1}$, which satisfy the following formularies,

$$\begin{aligned} \|V_{1,k+1} + \nabla_{\mathcal{Z}} Q(\mathcal{Z}_{k+1}, \mathbf{D}_k, \mathcal{X}_k)\|_F^2 &\leq \frac{\rho_k^z}{2} \|\mathcal{Z}_{k+1} - \mathcal{Z}_k\|_F^2, \\ \|V_{2,k+1} + \nabla_{\mathbf{D}} Q(\mathcal{Z}_{k+1}, \mathbf{D}_{k+1}, \mathcal{X}_k)\|_F^2 &\leq \frac{\rho_k^d}{2} \|\mathbf{D}_{k+1} - \mathbf{D}_k\|_F^2, \\ \|V_{3,k+1} + \nabla_{\mathcal{X}} Q(\mathcal{Z}_{k+1}, \mathbf{D}_{k+1}, \mathcal{X}_{k+1})\|_F^2 &\leq \frac{\rho_k^x}{2} \|\mathcal{X}_{k+1} - \mathcal{X}_k\|_F^2, \end{aligned}$$

where $V_{1,k+1} \in \partial F(\mathcal{Z})$, $V_{2,k+1} \in \partial \delta_{\mathcal{D}}(\mathbf{D})$, and $V_{3,k+1} \in \partial \delta_{\mathcal{X}}(\mathcal{X})$.

Proof. $F(\mathcal{Z})$ has the subgradient by **Theorem 3.7** of [44]. Thus, we have

$$\mathcal{R}(\mathbf{U}\text{diag}(\sigma_j(\text{bdiag}(\mathcal{Z})))\mathbf{V}^T) \in \partial F(\mathcal{Z}),$$

where \mathbf{U} and \mathbf{V} are the singular value decomposition matrices of $\text{bdiag}(\mathcal{Z})$ and $\text{diag}(\sigma_j(\text{bdiag}(\mathcal{Z})))$ denotes a diagonal matrix with diagonal entries $\sigma_1(\text{bdiag}(\mathcal{Z})), \dots, \sigma_{\min\{n_1, n_2\}}(\text{bdiag}(\mathcal{Z}))$. By the definition of M_1 , we have that

$$0 \in \partial F(\mathcal{Z}_{k+1}) + \nabla_{\mathcal{Z}} Q(\mathcal{Z}_{k+1}, \mathbf{D}_k, \mathcal{X}_k) + \rho_k^z(\mathcal{Z}_{k+1} - \mathcal{Z}_k).$$

Thus,

$$\begin{aligned} 0 &= \mathcal{R}(\mathbf{U}\text{diag}(\sigma_j(\text{bdiag}(\mathcal{Z}_{k+1})))\mathbf{V}^T) \\ &\quad - \beta \mathbf{D}_k^\top (\text{unfold}_3(\mathcal{X}_k) - \mathbf{D}_k \mathbf{Z}_{(3)k+1}) + \rho_k^z(\mathcal{Z}_{k+1} - \mathcal{Z}_k). \end{aligned}$$

Let

$$\begin{aligned} V_{1,k+1} &:= \beta \mathbf{D}_k^\top (\text{unfold}_3(\mathcal{X}_k) - \mathbf{D}_k \mathbf{Z}_{(3)k+1}) \\ &\quad - \rho_k^z(\mathcal{Z}_{k+1} - \mathcal{Z}_k) \in \partial F(\mathcal{Z}_{k+1}). \end{aligned}$$

It is clear that

$$\|V_{1,k+1} + \nabla_{\mathcal{Z}} Q(\mathcal{Z}_{k+1}, \mathbf{D}_k, \mathcal{X}_k)\|_F^2 = \rho_k^z \|\mathcal{Z}_{k+1} - \mathcal{Z}_k\|_F^2.$$

Consequently, there exists

$$\begin{aligned} 0 &\in \partial \delta_{\mathcal{D}}(\mathbf{D}_{k+1}) - \beta (\text{unfold}_3(\mathcal{X}_k) - \mathbf{D}_{k+1} \mathbf{Z}_{(3)k+1}) \mathbf{Z}_{(3)k+1}^\top \\ &\quad + \rho_k^d(\mathbf{D}_{k+1} - \mathbf{D}_k), \\ 0 &\in \partial \delta_{\mathcal{X}}(\mathcal{X}_{k+1}) + \beta (\mathcal{X}_{k+1} - \mathcal{Z}_{k+1} \times_3 \mathbf{D}_{k+1}) + \rho_k^x(\mathcal{X}_{k+1} - \mathcal{X}_k). \end{aligned}$$

Then, we define that

$$\begin{aligned} V_{2,k+1} &:= \beta (\text{unfold}_3(\mathcal{X}_k) - \mathbf{D}_{k+1} \mathbf{Z}_{(3)k+1}) \mathbf{Z}_{(3)k+1}^\top \\ &\quad - \rho_k^d(\mathbf{D}_{k+1} - \mathbf{D}_k) \in \partial \delta_{\mathcal{D}}(\mathbf{D}_{k+1}), \\ V_{3,k+1} &:= -\beta (\mathcal{X}_{k+1} - \mathcal{Z}_{k+1} \times_3 \mathbf{D}_{k+1}) \\ &\quad - \rho_k^x(\mathcal{X}_{k+1} - \mathcal{X}_k) \in \partial \delta_{\mathcal{X}}(\mathcal{X}_{k+1}). \end{aligned}$$

It can be seen that

$$\begin{aligned} \|V_{2,k+1} + \nabla_{\mathbf{D}} Q(\mathcal{Z}_{k+1}, \mathbf{D}_{k+1}, \mathcal{X}_k)\|_F^2 &\leq \rho_k^d \|\mathbf{D}_{k+1} - \mathbf{D}_k\|_F^2, \\ \|V_{3,k+1} + \nabla_{\mathcal{X}} Q(\mathcal{Z}_{k+1}, \mathbf{D}_{k+1}, \mathcal{X}_{k+1})\|_F^2 &\leq \rho_k^x \|\mathcal{X}_{k+1} - \mathcal{X}_k\|_F^2. \end{aligned}$$

The proof of relative error Lemma has been finished. \square

Now, we begin to establish our proof of the global convergency of the sequence generated by (24).

Theorem 2. The sequence generated by (24) is bounded, and it converges to a critical point of $L(\mathcal{Z}, \mathbf{D}, \mathcal{X})$.

Proof. It is easy to verify that Q is C^1 function with locally Lipschitz continuous gradient and F , $\delta_{\mathcal{D}}$, and $\delta_{\mathcal{X}}$ are proper and lower semi-continuous. Thus, L is a proper lower semi-continuous function. The nuclear norm and Frobenius norm are semialgebraic [45]. Additionally, the function with semi-algebraic sets is semialgebraic [45]. Thus the function L is a semi-algebraic function.

From Lemma 2, we have that the objective function value monotonically decreases. Firstly, we can see that the indicator function $\delta_{\mathcal{D}}(\mathbf{D}) = \Phi(\mathbf{D})$ should be 0 from its definition. Thus,

$$\|\mathbf{D}\|_F^2 = \sum_i \|\mathbf{D}(:, i)\|_2^2 = d,$$

which means $\{\mathbf{D}_k\}_{k \in \mathbb{N}}$ is bounded. Meanwhile, from the monotonic decreasing, the nonnegative terms $F(\mathcal{Z}) = \sum_{k=1}^d \|\mathcal{Z}^{(k)}\|_*$ and $Q(\mathcal{Z}, \mathbf{D}, \mathcal{X}) = \frac{\beta}{2} \|\mathcal{X} - \mathcal{Z} \times_3 \mathbf{D}\|_F^2$ are bounded. Then,

$$\|\mathcal{Z}\|_F^2 = \sum_{k=1}^d \|\mathcal{Z}^{(k)}\|_F^2 \leq \sum_{k=1}^d \|(\mathcal{Z}^{(k)})\|_*^2.$$

That is, $\{\mathcal{Z}_k\}_{k \in \mathbb{N}}$ is bounded. Next, from the triangle inequality, we have

$$\|\mathcal{X}\|_F - \|\mathcal{Z}\|_F \|\mathbf{D}\|_F \leq \|\mathcal{X}\|_F - \|\mathcal{Z} \times_3 \mathbf{D}\|_F \leq \|\mathcal{X} - \mathcal{Z} \times_3 \mathbf{D}\|_F.$$

This is equivalent to

$$\|\mathcal{X}\|_F \leq \|\mathcal{X} - \mathcal{Z} \times_3 \mathbf{D}\|_F + \|\mathcal{Z}\|_F \|\mathbf{D}\|_F.$$

Therefore, $\{\mathbf{X}_k\}_{k \in \mathbb{N}}$ is bounded.

By lemma 1, the sequence $\{\mathcal{Z}_k, \mathbf{D}_k, \mathcal{X}_k\}_{k \in \mathbb{N}}$ is a bounded sequence with the K-L property at each point.

Combining Lemma 2 and Lemma 3 with the above property of L , the process of updating in (24) is factually a special instance of the algorithm 4 described in [42]. Lemma 2 and Lemma 3 correspond to the (64)-(65)-(66) in [42]. Under these

TABLE I

PSNR, SSIM, AND UIQI OF RESULTS BY DIFFERENT METHODS WITH DIFFERENT SAMPLING RATES ON THE **VIDEO** DATA. THE **BEST**, THE **SECOND BEST**, AND THE **THIRD BEST** VALUES ARE RESPECTIVELY HIGHLIGHTED BY **RED**, **BLUE**, AND **GREEN** COLORS.

Video	SR	10%			20%			30%			40%			50%			Time (s)
		Method	PSNR	SSIM	UIQI												
<i>foreman</i>	Observed	3.96	0.010	0.006	4.48	0.017	0.016	5.05	0.025	0.027	5.72	0.035	0.040	6.51	0.047	0.056	0
	HaLRTC	20.10	0.511	0.328	23.88	0.700	0.562	26.77	0.812	0.699	29.35	0.883	0.790	31.85	0.928	0.853	4
	BCPF	23.58	0.610	0.458	26.03	0.723	0.586	27.27	0.769	0.638	27.98	0.793	0.666	28.42	0.808	0.682	829
	TRLRF	24.63	0.616	0.536	27.72	0.778	0.667	29.01	0.830	0.719	29.94	0.861	0.756	30.95	0.887	0.788	387
	TNN	23.71	0.606	0.489	26.90	0.748	0.640	29.13	0.824	0.720	31.28	0.880	0.783	33.47	0.921	0.835	30
	DCTNN	24.27	0.632	0.519	27.23	0.766	0.657	29.54	0.843	0.740	31.80	0.897	0.804	34.07	0.934	0.854	21
	FTNN	25.41	0.735	0.603	28.51	0.849	0.741	30.92	0.904	0.815	33.17	0.937	0.862	35.44	0.960	0.900	112
<i>carphone</i>	Observed	7.04	0.023	0.010	7.56	0.039	0.026	8.13	0.057	0.046	8.81	0.077	0.070	9.59	0.100	0.097	0
	HaLRTC	24.71	0.779	0.596	28.57	0.883	0.751	31.31	0.930	0.827	33.67	0.956	0.875	35.84	0.972	0.908	6
	BCPF	27.91	0.812	0.638	29.82	0.864	0.703	31.30	0.894	0.744	32.25	0.911	0.767	32.88	0.921	0.781	825
	TRLRF	29.44	0.841	0.691	32.10	0.905	0.767	33.58	0.930	0.805	34.71	0.945	0.832	35.63	0.955	0.853	414
	TNN	27.44	0.804	0.639	30.00	0.873	0.725	31.81	0.909	0.774	33.44	0.934	0.813	35.06	0.952	0.846	31
	DCTNN	28.21	0.829	0.669	30.64	0.889	0.747	32.37	0.920	0.792	33.96	0.943	0.829	35.57	0.959	0.859	21
	FTNN	29.16	0.880	0.740	31.58	0.927	0.815	33.43	0.949	0.855	35.03	0.963	0.884	36.61	0.973	0.906	118
<i>container</i>	Observed	4.87	0.011	0.007	5.38	0.021	0.018	5.96	0.032	0.031	6.63	0.045	0.047	7.42	0.060	0.064	0
	HaLRTC	25.96	0.855	0.614	30.58	0.935	0.779	34.98	0.970	0.879	39.56	0.986	0.937	44.54	0.994	0.969	6
	BCPF	28.97	0.880	0.629	33.38	0.926	0.707	35.77	0.944	0.748	37.81	0.954	0.777	38.66	0.960	0.795	875
	TRLRF	32.82	0.932	0.738	37.55	0.961	0.817	39.57	0.969	0.851	40.64	0.974	0.875	41.94	0.980	0.900	387
	TNN	30.04	0.909	0.715	35.55	0.963	0.853	38.81	0.979	0.905	41.55	0.986	0.934	44.01	0.991	0.954	29
	DCTNN	31.61	0.930	0.762	38.27	0.977	0.892	42.69	0.989	0.940	45.91	0.993	0.960	48.43	0.996	0.972	19
	FTNN	32.43	0.948	0.809	37.38	0.978	0.904	41.41	0.988	0.946	44.42	0.992	0.958	47.16	0.994	0.971	146
<i>highway</i>	Observed	3.52	0.010	0.003	4.04	0.015	0.008	4.61	0.020	0.014	5.28	0.027	0.021	6.07	0.034	0.029	0
	HaLRTC	28.80	0.854	0.604	31.55	0.909	0.730	33.57	0.937	0.797	35.26	0.954	0.844	36.83	0.966	0.880	5
	BCPF	29.96	0.840	0.593	32.10	0.879	0.664	33.17	0.897	0.693	34.16	0.912	0.716	34.57	0.918	0.729	714
	TRLRF	31.31	0.857	0.661	33.81	0.905	0.729	35.35	0.929	0.773	36.40	0.943	0.806	37.59	0.956	0.841	387
	TNN	30.19	0.852	0.631	32.07	0.893	0.704	33.57	0.917	0.753	34.90	0.936	0.794	36.26	0.951	0.832	26
	DCTNN	30.59	0.864	0.648	32.35	0.899	0.715	33.79	0.922	0.762	35.12	0.939	0.802	36.49	0.954	0.838	19
	FTNN	31.23	0.893	0.693	33.09	0.926	0.764	34.63	0.944	0.808	35.93	0.956	0.842	37.25	0.966	0.875	123
	DTNN	31.70	0.902	0.711	33.96	0.931	0.774	35.81	0.948	0.815	37.34	0.959	0.849	38.71	0.968	0.877	223

conditions, this proof conforms to Theorem 6.2 of [42]. Thus, the bounded sequence $\{\mathcal{Z}_k, \mathbf{D}_k, \mathcal{X}_k\}_{k \in \mathbb{N}}$ converges to a critical point of $L(\mathcal{Z}, \mathbf{D}, \mathcal{X})$. \square

Algorithm 1 is a direct multi-block generalization of (24). The proof of its convergence accords with the proof of Theorem 2 and can be easily obtained. Meanwhile, the above convergence analysis is more similar to the analysis in [42], being convenient for the verification of readers. Therefore, we establish the proof of Theorem 2 here.

IV. NUMERICAL EXPERIMENTS

In this section, we compare our method with other state-of-the-art methods. Compared methods consist of: one baseline Tucker-rank based method HaLRTC² [4], a Bayesian CP-factorization based method (BCPF³) [22], a tensor ring decomposition based method (TRLRF⁴) [32], a t-SVD based method (TNN⁵) [17], a DCT induced TNN minimization method (DCTNN⁶) [13], and a framelet represented TNN minimization method (FTNN⁷) [16]. We select four types of tensor data, including videos, HSIs, traffic data, and MRI data, to show that our method is adaptive to different types of data.

Since the algorithm of our method is a non-convex approach, the initialization of our algorithm is important. We use a simple linear interpolation strategy, which is employed in [46] and convenient to implement with low cost, to fill

in the missing pixels and obtaining \mathcal{X}_0 for our method. The normalized tubes of \mathcal{X}_0 are used to initialize the dictionary \mathbf{D} . Then, we fix $\mathcal{X} = \mathcal{X}_0$ and run 10 iterations of our method to initialize the \mathcal{Z}_0 with random inputs.

A. Video Data

In this subsection, we test our method for the video data completion and select four videos⁸ named “*foreman*”, “*carphone*”, “*highway*” and “*container*” of the size $144 \times 176 \times 50$ (height \times width \times frame) to conduct the comparisons. The sampling rate (SR) varies from 10% to 50%. We compute the peak signal-to-noise ratio (PSNR), the structural similarity index (SSIM) [47], and the universal image quality index (UIQI) [48] of the results by different methods. Higher values of these three quality metrics indicate better completion performances.

In Tab. I, we report the quantitative metrics of the results obtained by different methods and the average running time on the video data. From Tab. I, it can be found that the results by TRLRF are promising when the sampling rate is low. The performance of FTNN is better than TNN and DCTNN for the video “*foreman*”, while DCTNN exceeds FTNN and TNN for the video “*container*”. This reveals the predefined transformations lack flexibility. Meanwhile, with minor exceptions, our DTNN achieves the best performance for different sampling rates, illustrating the superior of the data adaptive dictionary.

Fig. 2 exhibits one frame of the results by different methods on the video data. From the enlarged area, it can be found that our DTNN well restores edges in “*foreman*” and “*highway*”,

²<https://www.cs.rochester.edu/~jliu/code/TensorCompletion.zip>

³<https://github.com/qbzhaoy/BCPF>

⁴<https://github.com/yuanlonghao/TRLRF>

⁵https://github.com/jamiezeminzhang/Tensor_Completion_and_Tensor_RPCA

⁶Implemented by ourselves based on the code of TNN

⁷<https://github.com/TaiXiangJiang/Framelet-TNN>

⁸Videos available at <http://trace.eas.asu.edu/yuv/>.

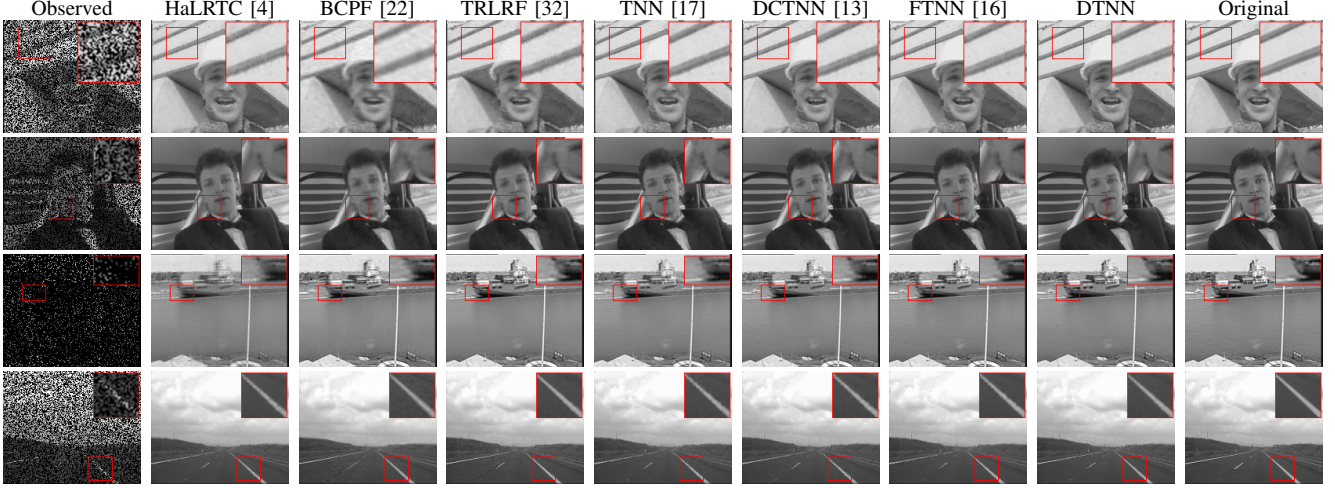


Fig. 2. One frame of the results on the **video** data. From top to bottom: The 22-th frame of “*foreman*” (SR = 50%), the 5-th frame of “*carphone*” (SR = 50%), the 39-th frame of “*container*” (SR = 10%), and the 48-th frame of “*highway*” (SR = 50%).

TABLE II

PSNR, SSIM, AND SAM OF RESULTS BY DIFFERENT METHODS WITH DIFFERENT SAMPLING RATES ON THE **HSI** DATA. THE **BEST**, THE **SECOND BEST**, AND THE **THIRD BEST** VALUES ARE RESPECTIVELY HIGHLIGHTED BY **RED**, **BLUE**, AND **GREEN** COLORS.

HSI	SR	5%			10%			20%			30%			40%			Time (s)
		Method	PSNR	SSIM	SAD	PSNR	SSIM	SAD									
Pavia City Center	Observed	12.19	0.020	1.355	12.43	0.036	1.254	12.94	0.070	1.110	13.52	0.108	0.993	14.18	0.149	0.887	0
	HaLRTC	22.95	0.596	0.126	27.67	0.835	0.095	35.68	0.970	0.048	43.11	0.994	0.024	51.84	0.999	0.010	25
	BCPF	29.12	0.850	0.100	33.00	0.927	0.077	37.71	0.970	0.051	39.51	0.980	0.043	40.12	0.982	0.041	3079
	TRLRF	33.75	0.936	0.068	37.03	0.967	0.051	38.97	0.978	0.044	40.13	0.983	0.040	41.10	0.986	0.036	1196
	TNN	26.08	0.739	0.147	32.49	0.918	0.099	38.18	0.968	0.064	41.89	0.982	0.048	45.01	0.989	0.037	98
	DCTNN	29.72	0.870	0.098	38.26	0.978	0.042	48.54	0.998	0.015	54.79	0.999	0.008	59.20	1.000	0.005	67
	FTNN	33.51	0.936	0.076	38.60	0.974	0.053	45.37	0.991	0.033	49.73	0.995	0.024	54.99	0.997	0.017	471
	DTNN	34.26	0.953	0.052	40.86	0.989	0.026	53.20	0.999	0.008	65.00	1.000	0.002	67.15	1.000	0.002	902
Washington DC Mall	Observed	12.45	0.028	1.353	12.68	0.053	1.254	13.19	0.108	1.110	13.77	0.169	0.993	14.44	0.234	0.887	0
	HaLRTC	23.24	0.713	0.208	29.36	0.906	0.125	38.21	0.983	0.062	44.76	0.996	0.034	49.67	0.999	0.020	43
	BCPF	28.65	0.877	0.155	32.06	0.939	0.118	34.75	0.964	0.093	35.70	0.971	0.086	35.98	0.972	0.083	5306
	TRLRF	31.74	0.934	0.121	33.64	0.955	0.102	34.98	0.966	0.091	35.86	0.972	0.084	36.73	0.976	0.078	1894
	TNN	22.34	0.657	0.260	30.19	0.915	0.142	36.56	0.974	0.085	40.10	0.987	0.062	43.03	0.992	0.047	163
	DCTNN	27.09	0.840	0.182	32.59	0.946	0.116	38.16	0.982	0.072	41.85	0.992	0.051	44.86	0.995	0.038	113
	FTNN	32.17	0.946	0.107	37.03	0.979	0.075	42.96	0.992	0.048	46.64	0.996	0.036	49.46	0.997	0.028	864
	DTNN	34.21	0.969	0.075	39.85	0.992	0.044	45.01	0.997	0.033	47.56	0.998	0.029	53.35	0.999	0.015	1853

the hair in “*carphone*”, and the ship’s outline in ‘*container*’. The homogeneous areas are also protected by our method. We can conclude that the visual effect of our method is the best.

B. Hyperspectral Images

In this subsection, 2 HSIs, i.e. a subimage of Pavia City Center dataset⁹ of the size $200 \times 200 \times 80$ (height \times width \times band), and a subimage of Washington DC Mall dataset¹⁰ of the size $256 \times 256 \times 191$ are adopted as the testing data. Since the redundancy between HSIs’ slices is so high that all the methods perform very well with SR=40%, we add the case with SR=5%. Thus, the sampling rates vary from 5% to 40%. Three numerical metrics, consisting of PSNR, SSIM, and the mean Spectral Angle Mapper (SAM) [49] are selected to quantitatively measure the reconstructed results. Lower values of SAM indicate better reconstructions.

In Tab. II, we show the quantitative comparisons of different methods on HSIs. FTNN and TRLRF perform well for the low sampling rate. We can also see that DCTNN and FTNN alternatively achieves the second best place in many cases, showing that DCT and framelet transformation fit the HSI data

better than DFT. For different metrics, our DTNN obtains the best values in all cases. As sampling rates arise, the superior of our method over compared methods is more evident. For example, when dealing with Pavia City Center, the margins are at least 10.21 dB and 7.95 dB for PSNR when SR is 40% and 50% , respectively. We attribute this to the fact that, the dictionary could be learned with better ability to express the data when the sampling rate is high.

We display the pseudo-color images (using three bands to compose the RGB channels) of the reconstructed HSIs in Fig. 3. The similarity of the color reflects the fidelity along the spectral direction, which is of vital importance in applications of HSIs. It can be found that the color distortion occurs in the results by TNN. From the enlarged orange and red boxes, we can see that DTNN outperforms compared methods considering the spatial structures and details.

C. Traffic Data

In this subsection, we test all the methods on the traffic data¹¹, which is provided by Grenoble Traffic Lab (GTL). A set of traffic speed data of 207 days (April 1, 2015 to

⁹http://www.ehu.eus/ccwintco/index.php?title=Hyperspectral_Remote_Sensing_Scenes

¹⁰<https://engineering.purdue.edu/biehl/MultiSpec/hyperspectral.html>

¹¹https://gtl.inrialpes.fr/data_download

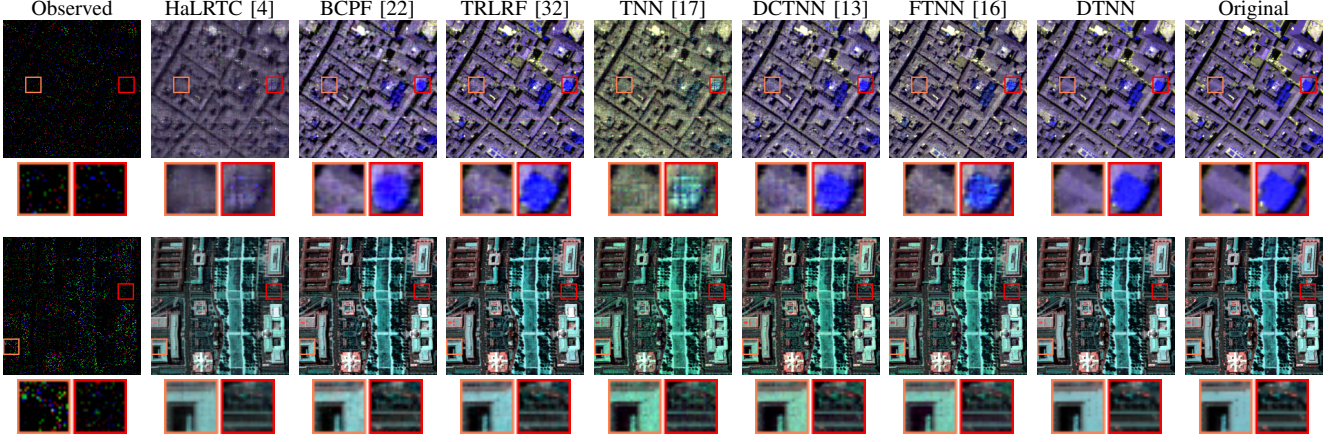


Fig. 3. The pseudo-color images and the corresponding enlarged areas of the results by different methods. Top: Pavia City Center (R-4 G-12 B-68) with SR = 5%. Bottom: Washington DC Mall (R-1 G-113 B-116) with SR = 10%.

TABLE III

RMSE AND MAPE OF RESULTS BY DIFFERENT METHODS WITH DIFFERENT SAMPLING RATES ON THE TRAFFIC DATA. THE **BEST**, THE **SECOND BEST**, AND THE **THIRD BEST** VALUES ARE RESPECTIVELY HIGHLIGHTED BY **RED**, **BLUE**, AND **GREEN** COLORS.

SR	5%		10%		15%		20%		25%		30%		Time (s)	
	Method	RMSE	MAPE	RMSE	MAPE	RMSE	MAPE	RMSE	MAPE	RMSE	MAPE	RMSE	MAPE	
Observed	0.9148	95.71 %		0.8942	91.44 %	0.8731	87.15 %	0.8514	82.87 %	0.8291	78.56 %	0.8061	74.26 %	0
HaLRTC	0.3592	17.51 %		0.3581	16.72 %	0.3575	16.26 %	0.3571	15.94 %	0.3569	15.68 %	0.3566	15.47 %	13
BCPF	0.3594	17.25 %		0.3576	16.45 %	0.3571	16.13 %	0.3568	15.97 %	0.3567	15.84 %	0.3566	15.76 %	218
TRLRF	0.1781	9.09 %		0.1753	8.62 %	0.1749	8.42 %	0.1747	8.29 %	0.1745	8.20 %	0.1744	8.08 %	107
TNN	0.0509	3.63 %		0.0387	2.75 %	0.0336	2.33 %	0.0304	2.03 %	0.0283	1.82 %	0.0267	1.65 %	27
DCTNN	0.0480	3.38 %		0.0387	2.71 %	0.0338	2.30 %	0.0315	2.07 %	0.0296	1.88 %	0.0278	1.70 %	18
FTNN	0.0452	3.33 %		0.0358	2.31 %	0.0316	1.96 %	0.0287	1.69 %	0.0265	1.49 %	0.0247	1.32 %	129
DTNN	0.0428	2.76 %		0.0354	2.19 %	0.0305	1.84 %	0.0278	1.60 %	0.0256	1.42 %	0.0237	1.26 %	264

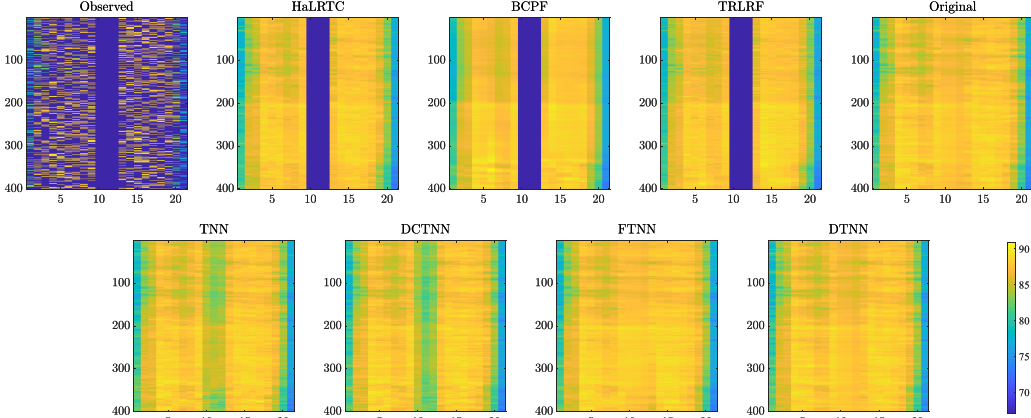


Fig. 4. The 88-th lateral slice of the reconstructions by different methods on the traffic data (SR = 30%).

October 24, 2015), 1440 time windows¹², and 21 detection points, is downloaded and constitutes a third-order tensor of the size $1440 \times 207 \times 21$. A subset of the data with the size $400 \times 200 \times 21$ is clipped as the ground truth complete testing data. We select the root mean square error (RMSE¹³) and the mean absolute percentage error (MAPE¹⁴) to quantitatively measure the quality of the results. Higher values of RMSE and MAPE indicate better reconstructions. After random sampling

¹²The sampling period is 1 minute, so there are $60 \times 24 = 1440$ time windows for each day.

¹³RMSE = $\sqrt{\left(\sum_{ijk} (\mathcal{X}_{ijk}^{\text{Rec}} - \mathcal{X}_{ijk}^{\text{GT}})^2\right) / n_1 n_2 n_3}$

¹⁴MAPE = $\frac{1}{n_1 n_2 n_3} \sum_{ijk} \left(\frac{|\mathcal{X}_{ijk}^{\text{Rec}} - \mathcal{X}_{ijk}^{\text{GT}}|}{\mathcal{X}_{ijk}^{\text{GT}}} \right) \times 100\%$. This index is a measure of prediction accuracy, usually expressing accuracy as a percentage.

the elements with $\text{SR} \in \{5\%, 10\%, 15\%, \dots, 30\%\}$, 3 adjacent frontal slices in a random location are set as unobserved. This is to simulate the situations in which some detectors are broken. The 200-th lateral slice of the observation is shown in the top-left of Fig. 4, the missing slices corresponding to the blue columns.

Tab. III gives the quantitative metrics of the results by different methods with different sampling rates. We can find that the capabilities of HaLRTC, BCPF, and TRLRF is limited and this phenomenon accord with the visual results shown in Fig. 4. The effectiveness of these three methods is severely affected due to the missing frontal slices. TNN and DCTNN get better metrics while their performance is also not well

TABLE IV

PSNR, SSIM, AND UIQI OF RESULTS BY DIFFERENT METHODS WITH DIFFERENT SAMPLING RATES ON THE **MRI** DATA. THE **best** AND THE **SECOND BEST** VALUES ARE RESPECTIVELY HIGHLIGHTED BY **boldface** AND underline.

SR	10%			20%			30%			40%			50%			Time (s)
	Method	PSNR	SSIM	UIQI	PSNR	SSIM	UIQI									
Observed	8.09	0.043	0.020	8.60	0.070	0.050	9.18	0.099	0.086	9.85	0.132	0.127	10.64	0.167	0.173	0
HaLRTC	18.34	0.436	0.349	22.48	0.651	0.606	26.01	0.794	0.756	29.19	0.880	0.840	32.13	0.931	0.889	11
TRLRF	23.89	0.637	0.606	25.48	0.720	0.682	26.36	0.760	0.722	27.17	0.794	0.756	28.06	0.825	0.786	921
BCPF	22.63	0.574	0.518	24.70	0.678	0.631	25.37	0.710	0.663	25.55	0.720	0.671	25.71	0.727	0.678	2430
TNN	22.41	0.577	0.550	27.12	0.789	0.757	30.01	0.874	0.833	32.55	0.922	0.876	35.01	0.953	0.905	60
DCTNN	23.79	0.644	0.617	27.63	0.808	0.773	30.56	0.888	0.844	33.15	0.932	0.885	35.62	0.960	0.911	45
FTNN	25.15	0.743	0.695	29.02	0.872	0.825	31.96	0.928	0.883	34.49	0.958	0.916	36.89	0.975	0.937	253
DTNN	27.19	0.835	0.790	31.03	0.917	0.870	33.65	0.949	0.902	35.83	0.966	0.920	37.91	0.978	0.934	568

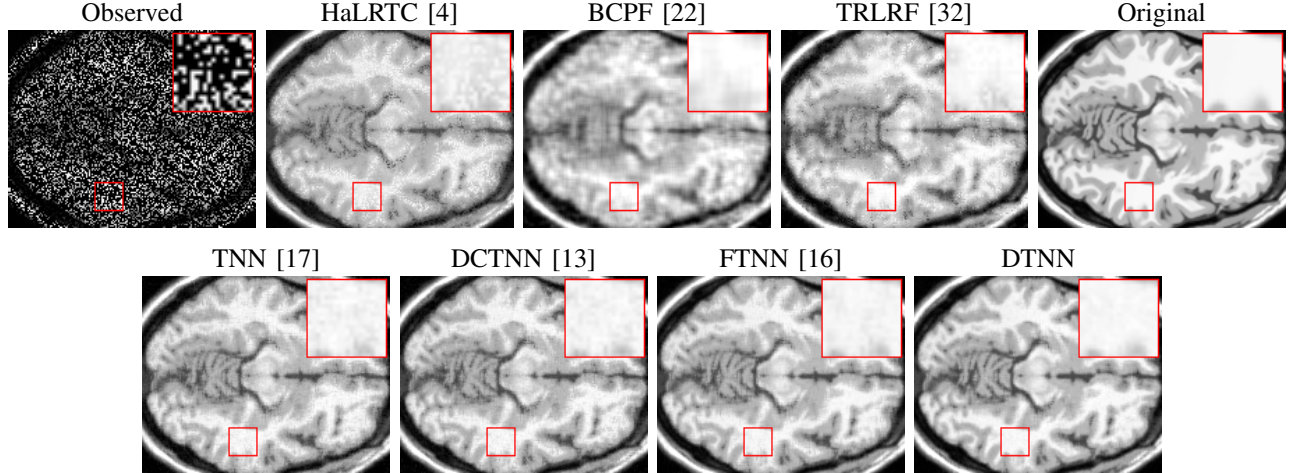


Fig. 5. The 61-th frontal slice of the results on the **MRI** data by different methods (SR = 30%).

considering the location of missing slices. FTNN and DTNN recover the rough structure of the missing slices and the metrics of their results also achieve the best and the second best places. The reconstruction of our DTNN in the area of missing slices is closer to the original data than FTNN.

D. MRI Data

In this section, all the methods are conducted on the MRI data¹⁵ of the size $142 \times 178 \times 121$. The sampling rates are set from 10% to 50%. Similar to the video data, we compute the mean values of PSNR, SSIM, and UIQI of each frontal slices and report them in Tab. IV. From Tab. IV, we can find that DTNN outperforms compared methods while DCTNN and FTNN alternatively obtain the second best values. Fig. 5 presents the 61-th frontal slice of the results by different methods. For the enlarged white manner area, which is smooth, the results by our DTNN is the cleanest compared with the results by other methods.

E. Discussions

1) *Sparsity VS low-rankness*: In this part, we discuss the situation where the objective function $\|\text{bdiag}(\mathcal{Z})\|_*$ in our model is replaced by a simple sparsity term such as $\|\mathcal{Z}\|_1$. After this, it is similar to the traditional dictionary learning methods with sparse constrained coefficients. We also use the multi-block proximal alternating minimization algorithm to

TABLE V
PSNR OF RESULTS BY DTNN AND DTNNs WITH DIFFERENT SAMPLING RATES ON THE **HSI** DATA PAVIA CITY CENTER.

SR	5%	10%	20%	30%	40%
DTNN	34.26	40.86	53.20	65.00	67.15
DTNN (sparsity)	17.48	23.00	34.78	46.48	61.14

solve this model. The algorithm is the similar to Algorithm 1, except for solving the \mathbf{Z}^i ($i = 1, 2, \dots, d$) subproblems. We update \mathbf{Z}_{k+1}^i with the soft thresholding as

$$\mathbf{Z}_{k+1}^i = \text{sign}(\mathbf{M}^{k,i}) \odot \left(|\mathbf{M}^{k,i}| - \frac{1}{\beta + \rho_k^z} \right)_+,$$

where \odot denotes the element-wise product and $|\cdot|$ means the absolute value. We use the same initializations as our DTNN. We use “DTNN (sparsity)” to denote the sparsity based method. The parameters of DTNN (Sparsity) are manually tuned for the best performances. Meanwhile, we enlarge ρ at the 15-th, 20-th, and 25-th iterations by multiplying the factor 1.5 and enlarge ρ by multiplying the factor 1.2 at each iteration from the 30-th iteration until satisfying the condition of convergence. We test DTNN (sparsity) on the HSI data Pavia City Center. We list the PSNR values of the results by our DTNN and DTNN (sparsity) in Tab. V. From Tab. V, it can be found that the performance of DTNN (sparsity) is inferior to DTNN. Especially, when the sampling rate is low, the PSNR values obtained by DTNN (sparsity) are poor.

¹⁵<https://brainweb.bic.mni.mcgill.ca/brainweb/selection>

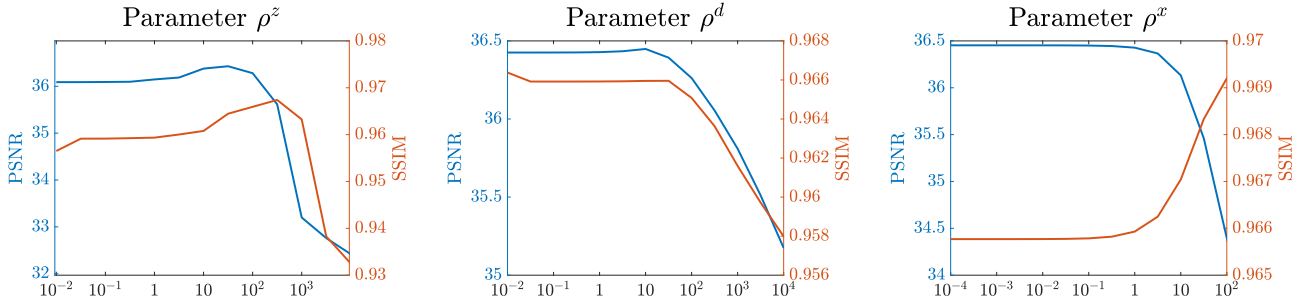


Fig. 6. The PSNR and SSIM values of our method with different ρ^z , ρ^d , and ρ^x on the video “foreman” (SR = 50%).

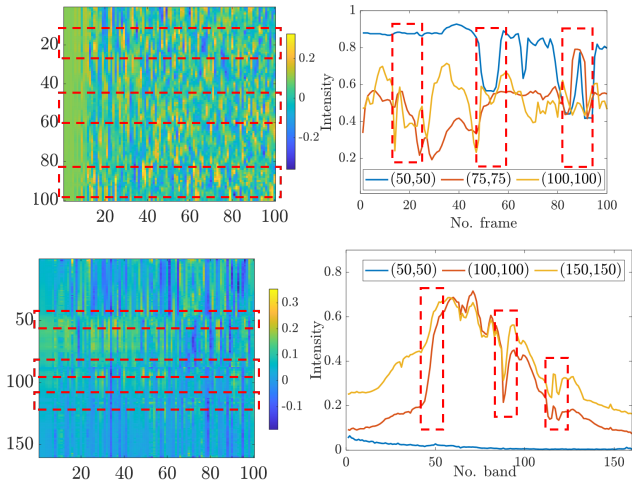


Fig. 7. The learned dictionaries (left) and the tubes of the original data (right). Top: the video “foreman”. Bottom: the HSI Pavia City Center.

This also supports our statement at the end of Sec. III-A that we need both the learned dictionary and the specific low-rank structure of the coefficients for the accurate completion of the data.

2) *Parameters*: Throughout all the experiments in this paper, the selected parameters of the proposed method are set as: $d = 5n_3$, $\beta = 10$, $\rho^z = 20$, $\rho^d = 1$, and $\rho^x = 1$. In the framework of the HQS algorithm, the penalty parameter ρ is required to reach infinite when iteration goes on. Therefore, we enlarge ρ at the 15-th, 20-th, and 25-th iterations by multiplying the factor 1.5 and enlarge ρ by multiplying the factor 1.2 at each iteration from the 30-th iteration until satisfying the condition of convergence.

As for the parameter d , we have also tested $d = 2n_3, 3n_3, 10n_3$. As d becomes larger, the performance is better. However, the performance of $d = 10n_3$ is only slightly better than that of $d = 5n_3$ but being much more time consuming. Thus, considering the tradeoff of the effectiveness and efficiency, we set $d = 5n_3$.

Next, to test the effects of ρ^z , ρ^d , and ρ^x , we take the video “foreman” as an example and set the sampling rate as 50%. Then, we alternately change each of them, keeping others the same as our default setting. We illustrate the PSNR and SSIM values with respect to different parameters in Fig. 6. From Fig. 6, we can see that the performance of our method is more sensitive to ρ^z . Our method could obtain satisfactory results

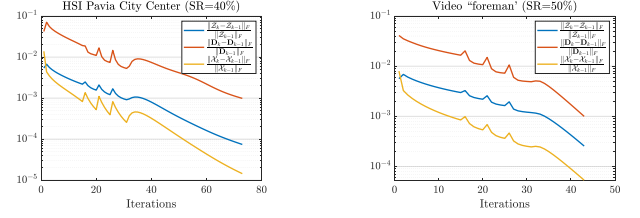


Fig. 8. The relative changes of the variables. Left: MRI data with SR=30%. Right: video data “foreman” with SR=50%.

with a wide range of ρ^d and ρ^x .

3) *Learned dictionaries*: In Fig. 7, we exhibit the first 100 columns of the learned dictionaries together with the plotting of three tubes of the original data. From the red boxes with dashed line, we can see that when the tubes, i.e., the vectors along the third dimension, of the original data fluctuate, the corresponding areas of the dictionaries’ atoms (columns) tend not to be smooth. This reflects that the dictionaries learned by our method is flexible and adaptive to different types of data.

4) *Convergency behaviors*: When the largest relative change of the variables, i.e., $\max\{\frac{\|\mathcal{Z}_k - \mathcal{Z}_{k-1}\|_F}{\|\mathcal{Z}_{k-1}\|_F}, \frac{\|\mathcal{D}_k - \mathcal{D}_{k-1}\|_F}{\|\mathcal{D}_{k-1}\|_F}, \frac{\|\mathcal{X}_k - \mathcal{X}_{k-1}\|_F}{\|\mathcal{X}_{k-1}\|_F}\}$, is smaller than 10^{-3} , we consider that our algorithm converges and stop the iterations. In Fig. 8, we present the relative changes with respect to the iterations in our experiments on the HSI data Pavia City Center and the video data “foreman”. Three obvious fluctuations in each curve are in accord with our parameter setting of enlarging ρ at the 15-th, 20-th, and 25-th iterations. The overall downward trend of the curves in Fig. 8 illustrates that our method converges quickly.

V. CONCLUSIONS

In this paper, we have introduced the data-adaptive dictionary and low-rank coding for third-order tensor completion. In the completion model, we have proposed to minimize the low-rankness of each tensor slice containing the coding coefficients. To optimize this model, we design a multi-block proximal alternating minimization algorithm, the sequence generated by which would globally converge to a critical point. Numerical experiments conducted on various types of real-world data show the superior of the proposed method.

As a future research work, we will consider how to use the proposed model and idea to analyze and study a tensor-based representation learning method for multi-view clustering. Here multi-view data as a third-order tensor expresses each tensorial

data point as a low rank representation of the learned learned dictionary basis.

ACKNOWLEDGMENT

The authors would like to thank the authors of [4, 17, 22, 32, 50] for their generous sharing of their codes. The authors would like to thank the support from Financial Intelligence and Financial Engineering Research Key Laboratory of Sichuan province.

REFERENCES

- [1] M. Bertalmio, G. Sapiro, V. Caselles, and C. Ballester, “Image inpainting,” in *the Annual Conference on Computer Graphics and Interactive Techniques (SIGGRAPH)*, 2000, pp. 417–424.
- [2] N. Komodakis, “Image completion using global optimization,” in *the IEEE Conference on Computer Vision and Pattern Recognition (CVPR)*, 2006, pp. 442–452.
- [3] T. Korah and C. Rasmussen, “Spatiotemporal inpainting for recovering texture maps of occluded building facades,” *IEEE Transactions on Image Processing*, vol. 16, no. 9, pp. 2262–2271, 2007.
- [4] J. Liu, P. Musialski, P. Wonka, and J. Ye, “Tensor completion for estimating missing values in visual data,” *IEEE Transactions on Pattern Analysis and Machine Intelligence*, vol. 35, no. 1, pp. 208–220, 2013.
- [5] R. Koller, L. Schmid, N. Matsuda, T. Niederberger, L. Spinoulas, O. Cossairt, G. Schuster, and A. Katsaggelos, “High spatio-temporal resolution video with compressed sensing,” *Optics express*, vol. 23, no. 12, p. 15992, 2015.
- [6] V. N. Varghees, M. S. Manikandan, and R. Gini, “Adaptive MRI image denoising using total-variation and local noise estimation,” in *the International Conference on Advances in Engineering, Science and Management (ICAESM)*, 2012, pp. 506–511.
- [7] L. Zhuang and J. M. Bioucas-Dias, “Fast hyperspectral image denoising and inpainting based on low-rank and sparse representations,” *IEEE Journal of Selected Topics in Applied Earth Observations and Remote Sensing*, vol. 11, no. 3, pp. 730–742, 2018.
- [8] J. M. Bioucas-Dias, A. Plaza, G. Camps-Valls, P. Scheunders, N. Nasrabadi, and J. Chanussot, “Hyperspectral remote sensing data analysis and future challenges,” *IEEE Geoscience and remote sensing magazine*, vol. 1, no. 2, pp. 6–36, 2013.
- [9] K. Braman, “Third-order tensors as linear operators on a space of matrices,” *Linear Algebra and its Applications*, vol. 433, no. 7, pp. 1241–1253, 2010.
- [10] M. E. Kilmer and C. D. Martin, “Factorization strategies for third-order tensors,” *Linear Algebra and its Applications*, vol. 435, no. 3, pp. 641–658, 2011.
- [11] Z. Zhang, G. Ely, S. Aeron, N. Hao, and M. Kilmer, “Novel methods for multilinear data completion and de-noising based on tensor-SVD,” in *the IEEE Conference on Computer Vision and Pattern Recognition (CVPR)*, 2014, pp. 3842–3849.
- [12] E. Kernfeld, M. Kilmer, and S. Aeron, “Tensor-tensor products with invertible linear transforms,” *Linear Algebra and its Applications*, vol. 485, pp. 545–570, 2015.
- [13] C. Lu, X. Peng, and Y. Wei, “Low-rank tensor completion with a new tensor nuclear norm induced by invertible linear transforms,” in *Proceedings of the IEEE Conference on Computer Vision and Pattern Recognition*, 2019, pp. 5996–6004.
- [14] W.-H. Xu, X.-L. Zhao, and M. Ng, “A fast algorithm for cosine transform based tensor singular value decomposition,” *arXiv preprint arXiv:1902.03070*, 2019.
- [15] G. Song, M. K. Ng, and X. Zhang, “Robust tensor completion using transformed tensor singular value decomposition,” *Numerical Linear Algebra with Applications*, vol. 27, no. 3, p. e2299, 2020.
- [16] T.-X. Jiang, M. K. Ng, X.-L. Zhao, and T.-Z. Huang, “Framelet representation of tensor nuclear norm for third-order tensor completion,” *IEEE Transactions on Image Processing*, vol. 29, pp. 7233–7244, 2020.
- [17] Z. Zhang and S. Aeron, “Exact tensor completion using t-SVD,” *IEEE Transactions on Signal Processing*, vol. 65, no. 6, pp. 1511–1526, 2017.
- [18] J. Q. Jiang and M. K. Ng, “Robust low-tubal-rank tensor completion via convex optimization,” in *Proceedings of the 28th International Joint Conference on Artificial Intelligence*, 2019, pp. 2649–2655.
- [19] A. Wang, X. Song, X. Wu, Z. Lai, and Z. Jin, “Robust low-tubal-rank tensor completion,” in *IEEE International Conference on Acoustics, Speech and Signal Processing (ICASSP)*. IEEE, 2019, pp. 3432–3436.
- [20] H. A. Kiers, “Towards a standardized notation and terminology in multiway analysis,” *Journal of Chemometrics: A Journal of the Chemometrics Society*, vol. 14, no. 3, pp. 105–122, 2000.
- [21] C. J. Hillar and L.-H. Lim, “Most tensor problems are NP-hard,” *Journal of the ACM*, vol. 60, no. 6, pp. 1–39, 2013.
- [22] Q. Zhao, L. Zhang, and A. Cichocki, “Bayesian CP factorization of incomplete tensors with automatic rank determination,” *IEEE Transactions on Pattern Analysis and Machine Intelligence*, vol. 37, no. 9, pp. 1751–1763, 2015.
- [23] Z. Han, Y. Wang, Q. Zhao, D. Meng, L. Lin, Y. Tang *et al.*, “A generalized model for robust tensor factorization with noise modeling by mixture of gaussians,” *IEEE transactions on neural networks and learning systems*, vol. 29, no. 11, pp. 5380–5393, 2018.
- [24] Q. Zhao, G. Zhou, L. Zhang, A. Cichocki, and S.-I. Amari, “Bayesian robust tensor factorization for incomplete multiway data,” *IEEE transactions on neural networks and learning systems*, vol. 27, no. 4, pp. 736–748, 2016.
- [25] L. R. Tucker, “Some mathematical notes on three-mode factor analysis,” *Psychometrika*, vol. 31, no. 3, pp. 279–311, 1966.
- [26] X. Zhang, “A nonconvex relaxation approach to low-rank tensor completion,” *IEEE Transactions on Neural Networks and Learning Systems*, vol. 30, no. 6, pp. 1659–1671, 2018.
- [27] I. V. Oseledets, “Tensor-train decomposition,” *SIAM Journal on Scientific Computing*, vol. 33, no. 5, pp. 2295–2317, 2011.
- [28] J. A. Bengua, H. N. Phien, H. D. Tuan, and M. N. Do, “Efficient tensor completion for color image and video recovery: Low-rank tensor train,” *IEEE Transactions on Image Processing*, vol. 26, no. 5, pp. 2466–2479, 2017.
- [29] R. Dian, S. Li, and L. Fang, “Learning a low tensor-train rank representation for hyperspectral image super-resolution,” *IEEE transactions on neural networks and learning systems*, vol. 30, no. 9, pp. 2672–2683, 2019.
- [30] Y. Liu, J. Liu, and C. Zhu, “Low-rank tensor train coefficient array estimation for tensor-on-tensor regression,” *IEEE Transactions on Neural Networks and Learning Systems*, 2020.
- [31] Q. Zhao, G. Zhou, S. Xie, L. Zhang, and A. Cichocki, “Tensor ring decomposition,” *arXiv preprint arXiv:1606.05535*, 2016.
- [32] L. Yuan, C. Li, D. Mandic, J. Cao, and Q. Zhao, “Tensor ring decomposition with rank minimization on latent space: An efficient approach for tensor completion,” in *Proceedings of the AAAI Conference on Artificial Intelligence*, vol. 33, 2019, pp. 9151–9158.
- [33] J. Yu, G. Zhou, C. Li, Q. Zhao, and S. Xie, “Low tensor-ring rank completion by parallel matrix factorization,” *IEEE transactions on neural networks and learning systems*, 2020 (DOI:10.1109/TNNLS.2020.3009210).
- [34] Z. Long, Y. Liu, L. Chen, and C. Zhu, “Low rank tensor completion for multiway visual data,” *Signal Processing*, vol. 155, pp. 301–316, 2019.
- [35] Q. Song, H. Ge, J. Caverlee, and X. Hu, “Tensor completion algorithms in big data analytics,” *ACM Transactions on Knowledge Discovery from Data (TKDD)*, vol. 13, no. 1, p. 6, 2019.
- [36] M. E. Kilmer, K. Braman, N. Hao, and R. C. Hoover, “Third-

order tensors as operators on matrices: A theoretical and computational framework with applications in imaging,” *SIAM Journal on Matrix Analysis and Applications*, vol. 34, no. 1, pp. 148–172, 2013.

[37] D. L. Donoho, “For most large underdetermined systems of linear equations the minimal ℓ_1 -norm solution is also the sparsest solution,” *Communications on Pure and Applied Mathematics: A Journal Issued by the Courant Institute of Mathematical Sciences*, vol. 59, no. 6, pp. 797–829, 2006.

[38] Y. Peng, D. Meng, Z. Xu, C. Gao, Y. Yang, and B. Zhang, “Decomposable nonlocal tensor dictionary learning for multispectral image denoising,” in *Proceedings of the IEEE Conference on Computer Vision and Pattern Recognition*, 2014, pp. 2949–2956.

[39] C. Bao, H. Ji, Y. Quan, and Z. Shen, “Dictionary learning for sparse coding: Algorithms and convergence analysis,” *IEEE transactions on pattern analysis and machine intelligence*, vol. 38, no. 7, pp. 1356–1369, 2015.

[40] M. Aharon, M. Elad, and A. Bruckstein, “K-SVD: An algorithm for designing overcomplete dictionaries for sparse representation,” *IEEE Transactions on signal processing*, vol. 54, no. 11, pp. 4311–4322, 2006.

[41] J.-F. Cai, E. J. Candès, and Z. Shen, “A singular value thresholding algorithm for matrix completion,” *SIAM Journal on Optimization*, vol. 20, no. 4, pp. 1956–1982, 2010.

[42] H. Attouch, J. Bolte, and B. F. Svaiter, “Convergence of descent methods for semi-algebraic and tame problems: Proximal algorithms, forward-backward splitting, and regularized gauss–seidel methods,” *Mathematical Programming*, vol. 137, no. 1, pp. 91–129, 2013.

[43] J. Bolte, A. Daniilidis, A. Lewis, and M. Shiota, “Clarke subgradients of stratifiable functions,” *SIAM Journal on Optimization*, vol. 18, no. 2, pp. 556–572, 2007.

[44] A. S. Lewis and H. S. Sendov, “Nonsmooth analysis of singular values-part II: Applications,” *Set-Valued Analysis*, vol. 13, no. 3, pp. 243–264, 2005.

[45] J. Bolte, S. Sabach, and M. Teboulle, “Proximal alternating linearized minimization for nonconvex and nonsmooth problems,” *Mathematical Programming*, vol. 46, no. 1, pp. 459–494, 2014.

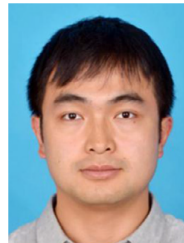
[46] N. Yair and T. Michaeli, “Multi-scale weighted nuclear norm image restoration,” in *Proceedings of the IEEE Conference on Computer Vision and Pattern Recognition*, 2018, pp. 3165–3174.

[47] Z. Wang, A. C. Bovik, H. R. Sheikh, and E. P. Simoncelli, “Image quality assessment: from error visibility to structural similarity,” *IEEE Transactions on Image Processing*, vol. 13, no. 4, pp. 600–612, 2004.

[48] Z. Wang and A. C. Bovik, “A universal image quality index,” *IEEE signal processing letters*, vol. 9, no. 3, pp. 81–84, 2002.

[49] R. H. Yuhas, J. W. Boardman, and A. F. Goetz, “Determination of semi-arid landscape endmembers and seasonal trends using convex geometry spectral unmixing techniques,” in *JPL, Summaries of the 4th Annual JPL Airborne Geoscience Workshop*, vol. 1, 1993, pp. 147–149.

[50] C. Lu, *Tensor-Tensor Product Toolbox*, Carnegie Mellon University, June 2018, <https://github.com/canyilu/tproduct>.



Tai-Xiang Jiang received the B.S., Ph.D. degrees in mathematics and applied mathematics from the University of Electronic Science and Technology of China (UESTC), Chengdu, China, in 2013. He is currently a lecturer with the School of Economic Information Engineering, Southwestern University of Finance and Economics. His research interests include sparse and low-rank modeling, tensor decomposition and multi-dimensional image processing. <https://sites.google.com/view/taixiangjiang/>



Xi-Le Zhao received the M.S. and Ph.D. degrees from the University of Electronic Science and Technology of China (UESTC), Chengdu, China, in 2009 and 2012. He is currently a Professor with the School of Mathematical Sciences, UESTC. His main research interests are focused on the models and algorithms of high-dimensional image processing problems.



Hao Zhang received the B.S. degrees in the college of science from the Sichuan Agricultural University (SAU), Yaan, China, in 2018. He is currently pursuing the M.S. degree with the School of Mathematical Sciences, University of Electronic Science and Technology of China (UESTC), Chengdu, China. His research interests are modeling and algorithm for high-order data recovery based on the low rank prior of tensors.



Michael K. Ng is the Director of Research Division for Mathematical and Statistical Science, and Chair Professor of Department of Mathematics, the University of Hong Kong, and Chairman of HKU-TCL Joint Research Center for AI. His research areas are data science, scientific computing, and numerical linear algebra.